Effects of the Large Magellanic Cloud on the Local Dark Matter Distribution in the Milky Way: Insights from the Auriga Simulation

by

Nima Ronaghikhameneh

A thesis submitted in partial fulfillment of the requirements for the degree of

Master of Science

Department of Phyiscs

University of Alberta

Abstract

This thesis investigates the Large Magellanic Cloud's (LMC) influence on the Milky Way's local dark matter distribution, focusing on implications for dark matter direct detection. Using state-of-the-art Auriga magneto-hydrodynamical simulations with an LMC-like system, we study the dark matter distribution in the Solar neighborhood during different phases of the LMC's orbit around the Milky Way. Our findings show that dark matter particles from the LMC analogue dominate the high speed tail of the local dark matter velocity distribution, confirming earlier Milky Way-LMC system simulations. The LMC's motion significantly accelerates native Milky Way dark matter particles in the Solar neighborhood, creating a distinct peak in the dark matter velocity distribution, particularly for speeds over 500 km/s with respect to the center of the Milky Way-like galaxy.

Simulations of potential signals in upcoming xenon, germanium, and silicon direct detection experiments reveal that the LMC's presence shifts expected direct detection exclusion limits towards smaller cross sections, especially for low mass dark matter. This highlights the LMC's critical role in future dark matter detection studies. We estimate the local dark matter density to be between $[0.21 - 0.60]$ GeV/cm^3, influenced by the prevalence of LMC dark matter particles in the Solar neighborhood and the Sun's relative position to the LMC in simulations. The outcomes contribute significantly to our understanding of the LMC's role in influencing the local dark matter distribution and the broader dynamics of dark matter particles in galactic environments.

Preface

This thesis is a comprehensive exploration of the effect of the Large Magellanic Cloud on the local dark matter distribution in the Milky Way, a topic that embodies both individual and collective academic endeavors. The content within is structured to precisely acknowledge the contributions of each collaborator.

Dr. Nassim Bozorgnia has led the research efforts, bringing forth significant insights and direction to the study. Chapter 2 is the original contribution of Adam Smith-Orlik, Dr. Nassim Bozorgnia, and Dr. Marius Cautun, whose joint expertise has been instrumental in establishing the research groundwork. Chapter 3 further showcases the collaborative synergy between Adam Smith-Orlik and Dr. Bozorgnia. Section 4.1 is a collective effort of Adam Smith-Orlik, Dr. Bozorgnia, and Dr. Cautun, reflecting their shared vision and comprehensive understanding of the subject. In addition to these efforts, I have actively contributed to the discussions and analysis of the results presented in these chapters and sections. Sections 4.2 to 4.5 are a joint endeavor among Adam Smith-Orlik, myself (Nima Ronaghi), and Dr. Bozorgnia, culminating in a multi-faceted and thorough examination of the topic. Chapter 5, which represents my work, Nima Ronaghi, offers personal insights and contributions to the broader research field.

Additionally, this research has been enriched by the contributions of other collaborators, whose diverse perspectives and expertise have significantly enhanced the study.

I am immensely proud to acknowledge that the contents of this thesis have been published in the Journal of Cosmology and Astroparticle Physics (Adam Smith-Orlik et al JCAP10(2023)070), a milestone that underscores our collective contribution to the scientific community.

The completion of this thesis is not merely an academic accomplishment but also a reflection of the collaborative spirit and dedication of my colleagues. Their invaluable support has been a cornerstone of this endeavor. I extend my heartfelt gratitude to all those who have been part of this significant academic journey.

To my parents

For being my first teachers and lifelong inspirations

Acknowledgements

I would like to express my profound gratitude to my advisor, Dr. Nassim Bozorgnia, for her exceptional guidance, patience, and invaluable expertise throughout this journey. Her mentorship has been a cornerstone of my academic and personal growth.

My sincere appreciation also goes to Adam Smith-Orlik for his invaluable collaboration and wisdom. His dedication and keen insights have greatly enriched our research and played a pivotal role in the successful realization of this thesis.

Contents

List of Tables

List of Figures

Chapter 1

Introduction

The undefined characteristics of dark matter remain a notable conundrum in the field of physics. An array of data, predominantly gathered from astrophysical and cosmological studies on the gravitational interaction of ordinary matter, points to an unseen type of matter. Astonishingly, this matter seems to have more mass than ordinary matter - as described by the trusted standard model of particle physics - by about five times. However, understanding dark matter solely through its gravitational effects is insufficient since all matter types share these interactions. The key to unlocking the minute properties of dark matter lies in pinpointing yet-to-be-discovered behaviors. This will require formulating solid theories, creating detailed experiment designs and observational methods, as well as carrying out meticulous data analyses to sift out any "new physics" hints in vast data collections amidst potentially misleading factors.

Despite the complexities, the quest to pinpoint what dark matter is might be the most encouraging path to enhance our comprehension of particle physics. By giving a clear definition to dark matter and formulating a core theory that envelops both ordinary matter and dark matter, along with their interplays, we could potentially unravel solutions to profound theoretical dilemmas. Given that dark matter constitutes the primary portion of the universe's matter, it plays a fundamental role in modeling the universe and the motions of galaxies and clusters of galaxies. Hence, the investigation of dark matter is exceedingly intriguing, and gaining a clear understanding of its unique aspects is essential

for our grasp of the universe's evolution.

This chapter serves as a preliminary overview of the topic of dark matter, offering a concise introduction. Specifically, section 1.1 outlines the observational evidence supporting the existence of dark matter, whereas section 1.2 introduces various hypothesized candidates of dark matter, a discussion on Weakly Interacting Massive Particles (WIMPs), methods of detecting dark matter, and delivers a display of the most recent findings and the current status of dark matter direct detection experiments. Section 1.4, focuses on the existing cosmological simulations that map the evolution of matter in the universe. The main focus of this research, the effect of the LMC on the local dark matter distribution, is outlined in section 1.5. The structure of this thesis is presented in section 1.6, providing a road map for the subsequent chapters.

1.1 The evidence for dark matter

1.1.1 Cosmic Microwave Background

The Cosmic Microwave Background (CMB) is the residual thermal radiation left over from the time of recombination in Big Bang cosmology, providing a snapshot of the universe when it was only about 380,000 years old. This radiation, which is uniform across the sky, contains minute fluctuations that are crucial for understanding the early universe. In the standard model of cosmology, Λ-Cold Dark Matter (Λ-CDM), "Cold Dark Matter" refers to a form of dark matter that moves slowly compared to the speed of light, playing a vital role in structure formation in the universe. This model significantly aligns with the available cosmic data, thereby underlining the key role of dark matter in interpreting fluctuations in the CMB data. The gravitational fluctuations caused by local high and low density regions of CDM incite oscillations in the combined baryon-photon fluid. These fluctuations result in observable temperature differences displayed as acoustic peaks in the CMB power spectrum. By analyzing the relative prominence of these peaks, we can estimate the proportion between matter and radiation, enabling us to calculate the density of dark matter in the universe. Latest studies [3] suggest a universe that seems

flat, and present values for $\Omega_b h^2$ and $\Omega_m h^2$ at a 68% confidence interval as 0.02233 ± 0.00015 and 0.1428 ± 0.0011, respectively. Here, 'h' stands for the Hubble constant expressed in units of 100 km/(s.Mpc), and Ω_b and Ω_m signify the density ratios of baryonic matter and all matter, respectively. Hence, it is inferred that dark matter is about five times as abundant as ordinary matter.

1.1.2 Rotation curves

Observations of stars and galaxies hint at the presence of a non-baryonic form of matter influencing their behavior. One can deduce a galaxy's mass by looking at its rotation curve, which essentially represents the pattern of its circular velocity.

An essential principle in this context is that star and gas velocity within a galaxy's gravitational pull is inherently linked to the gravitational force it experiences, which is determined by the galaxy's internal mass relative to the orbit. This principle underpins our most direct evidence for dark matter, which comes from gauging the circular velocity of stars and gas within galaxies.

Given the extremely rare occurrence of collisions of stars or gas in the galactic disk, it is clear that a galaxy's movement is largely dictated by gravitational forces. Using the principles of Newtonian gravity, we can calculate the circular velocity of stars,

$$v_c = \sqrt{\frac{GM_r}{r}}, \tag{1.1}$$

where G is the universal gravitational constant, while M_r represents the mass of the galaxy enclosed within a galactocentric sphere of radius r. One can assemble the mass distribution of a galaxy by evaluating the circular velocities of a multitude of stars and the gas situated at various distances from the galaxy's center. Figure 1.1 illustrates this with an example of an observed rotation curve for the Milky Way (MW) galaxy along with theoretical predictions. The same pattern has been observed in a broad range of galaxies and clusters of galaxies. When we consider these observations without factoring in dark matter, the contrast between theoretical expectations and actual observations is significant. The flattened velocity curves at large distances from the

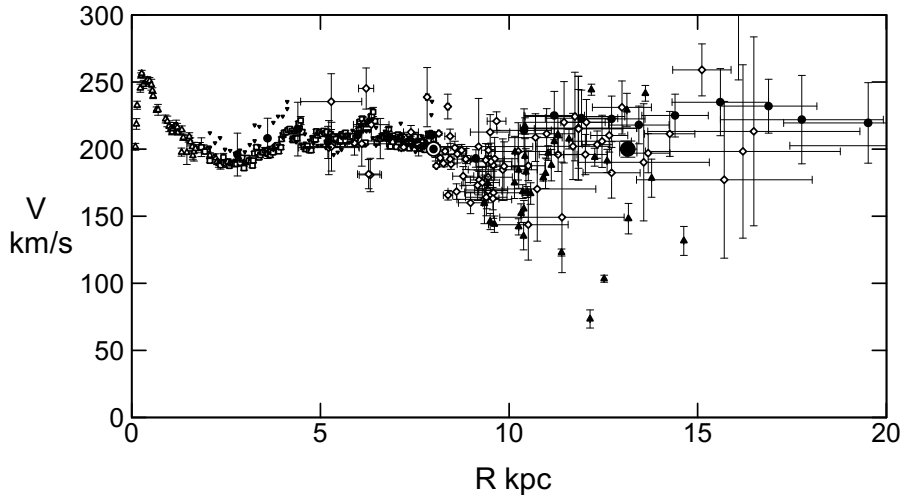

Figure 1.1: Observed circular velocities representing the rotation curve of the Milky Way galaxy. (figure from ref. [61])

galactic center can be explained by a mass distribution of $M(r) \propto r$, pointing to the presence of an unseen form of matter extending beyond the galaxy's disk, known as the dark matter halo.

While galaxy rotation curves offer evidence, they merely represent gravitational anomalies and don't definitively establish the existence of "dark" matter. Rather than indicating the presence of extra matter, these rotation curves might be pointing us toward modifications of the law of gravity. The latter is referred to as MOdified Newtonian Dynamics (MOND) theories, which introduces an alternative explanation to the rotation curve problem. (for more details see ref. [27]).

1.1.3 Gravitational lensing

Gravitational lensing [9] offers yet another window into the potential existence of dark matter. This phenomenon occurs when a massive celestial mass is positioned between the observer on Earth and the subject of observation. The pathway of light rays, when passing by this massive object, deviates due to the disturbance the object causes in spacetime. Consequently, the observer may notice either multiple images (referred to as, strong lensing) or some

Figure 1.2: The Bullet Cluster; Using the Chandra X-ray observatory, hot gas, or baryonic matter, in two colliding clusters was detected and depicted in pink. An image combining data from Magellan and Hubble displays galaxies in orange and white. Gravitational lensing, represented in blue, shows most of the clusters' matter is separate from the baryonic matter, indicating the prevalence of dark matter. (Credit: X-ray: NASA/CXC/CfA/M.Markevitch et al.; Optical: NASA/STScI; Magellan/U.Arizona/D.Clowe et al.; Lensing Map: NASA/STScI; ESO WFI; Magellan/U.Arizona/D.Clowe et al.)

deformation (weak lensing) in the visual representation of the observed object. The degree of this distortion can be used to deduce the mass of the object that is influencing spacetime along the observer's line of sight.

By comparing the mass distribution with the pattern of electromagnetic emissions, we can detect the existence of dark matter, as demonstrated in familiar instances like the "Bullet Cluster", as depicted in figure 1.2. The figure showcases pink and blue shadows, representing the peaks of X-ray emission and mass distribution, respectively. The blue shadow aligns with the area where galaxies reside, suggesting that the majority of the matter in the cluster, which is dark, does not interact like baryonic matter. Calculations pertaining to the total mass reveal an excess beyond what is comprised of galaxies and stars, which implies the existence of dark matter. If we operate under the premise that dark matter consists of particles, we can use these observations to set upper limits on the self-interaction cross section of dark matter [53].

1.1.4 Large scale structure

The structure we see in the universe are essentially the end product of initial density fluctuations set into motion by inflation in the Universe's early stages, leading to gravitational instabilities. By studying the evolution of these density disturbances, we can foresee their growth over time. To mirror the observations, it is found that these matter density fluctuations need to commence their growth prior to the era of recombination. However, the close interaction between baryonic matter and radiation opposes gravity, preventing density field fluctuations for baryonic matter from growing before recombination. Therefore, it becomes necessary to have a component of matter that is non-baryonic and has negligible interactions with radiation.

The concept of non-baryonic dark matter, underpinned by theories of large cosmological structure evolution, has received empirical support through N-body simulations. These simulations trace the progression of structure formation from initial conditions, which are based on data from the CMB. The statistical congruence between extensive systems of galaxy observations and their simulated N-body counterparts is viewed as a triumph for the ΛCDM model. As a result, the value of N-body simulations has been elevated, now serving as a potent tool for predicting the traits of the matter power spectrum in relation to diverse scales and dark matter particle paradigms.

1.2 Particle candidates of dark matter

The nature of dark matter is a mystery that science has yet to unravel fully. Some suggest alternative solutions to explain the discrepancy observed in astrophysical objects' mass, including hidden baryonic matter or modified gravity. Nonetheless, the proposition that dark matter could consist of an assortment of unobserved particles that exist beyond the realm of the standard model remains a prominent theory. This hypothetical collection of particles is often collectively referred to as the "dark sector".

To qualify as potential components of the dark sector, the dark matter candidate particles must meet a basic set of criteria. They should be elec-

trically neutral and have extremely feeble interactions with ordinary matter. Their interaction level, if it exists, should be comparable to or weaker than the weak scale; otherwise, they would have been detected by now. These particles need to exhibit stability on a cosmological scale, meaning they should not have decayed over the extensive span of cosmic time. Additionally, these particles must be non-relativistic to comply with the predictions of the ΛCDM model and the mechanisms of large-scale structure formation [50].

Various candidates have been proposed to fill the role of dark matter, such as CDM, axions, fuzzy dark matter, and warm dark matter, each with distinct properties and implications for cosmology and particle physics. Fuzzy dark matter, for instance, is characterized by its suppression of structure growth on small scales and potential signatures in the 21-cm signal due to its delaying effects on cosmic dawn and the epoch of reionization [57][7]. Warm dark matter, on the other hand, naturally reproduces astronomical observations at both small and large scales and may be detectable in beta decay [64]. However, this discussion will focus specifically on WIMPs, a class of particles that has garnered significant attention in both theoretical predictions and experimental searches.

1.2.1 WIMPs

Within the spectrum of potential dark matter candidates, WIMPs are among the most notable. As indicated by its designation, it is a hypothetical particle, neutral and stable, with a mass ranging from a few GeV/c^2 to several TeV/c^2. Its interaction with ordinary matter is theorized to occur at or below the weak scale.

The standard proposition for the origin of WIMP dark matter is rooted in the early Universe's high-temperature conditions. During this epoch, it is assumed that WIMPs were in thermal equilibrium with the plasmatic ordinary matter due to the intense heat [30]. However, as the Universe continued to expand and cool, lighter particles lacked the requisite kinetic energy to generate dark matter. Concurrently, WIMPs became so sparse that annihilation was no longer feasible, a phenomenon termed "freeze-out".

It is also noteworthy that the existence of WIMPs is a natural expectation in various theoretical frameworks that go beyond standard model. These include but are not limited to, theories such as super-symmetry models (SUSY) and models incorporating extra dimensions (see ref. [40] for more details).

1.2.2 WIMPs searches

Globally, a multitude of initiatives is underway that aim to uncover the elusive dark matter particles. These efforts can essentially be bucketed into three main tactics:

1. The first involves experiments focused on **direct detection**, where the objective is to capture the interactions between dark matter particles and atomic nuclei in underground laboratories.

2. The second strategy for detecting dark matter involves high-energy **accelerators**, such as the Large Hadron Collider (LHC), where standard model particles are accelerated to high speeds and collide. These collisions are investigated for signs of "missing energy," indicative of dark matter particles produced and then escaping detection due to their weak interaction with ordinary matter.

3. Lastly, the third approach in dark matter research involves **indirect detection** experiments, which seek evidence of dark matter annihilation or decay through diverse residues. Gamma-ray detectors, such as Fermi-LAT [10], probe for dark matter annihilation signals in gamma rays, while cosmic-ray measurements focus on potential dark matter decay or annihilation byproducts like antimatter. Neutrino detectors aim to detect high-energy neutrinos resulting from dark matter interactions, particularly from celestial bodies, offering another avenue for indirect dark matter detection [54].

Detailed discussions about direct methods of detecting dark matter particles are to follow in the subsequent sections.

Direct detection experiments

The hunt for dark matter, specifically WIMPs, has led to an array of unique direct detection experimental designs utilizing various materials.

These designs include [13]:

- **High-purity scintillator crystals**, predominantly NaI(Tl) and CsI(Tl), are used to create large target masses. These designs are generally simple and can operate stably over long periods. The high mass numbers of Iodine and Cesium enhance sensitivity to spin-independent interactions. However, they also possess a significant intrinsic background level and lack electronic recoil rejection. Instead, these designs focus on exploiting the annual modulation signature to identify a dark matter signal.

- **Germanium and silicon semiconductor** ionization detectors aim to detect dark matter-induced charge signals. These detectors stand out for their superior energy resolution due to the minimum energy required to generate an electron-hole pair. However, they are limited in size due to the high electronic noise generated by the diodes' capacitance.

- **Crystalline cryogenic** detectors, or bolometers, measure either heat or athermal phonon signals resulting from particle interactions. These detectors operate at cryogenic temperatures to achieve good sensitivity and use dielectric crystals with good phonon-transport properties.

- **Noble gases** like argon and xenon serve as excellent scintillators and ionization agents, primarily in their liquid state. They enable the construction of dense and compact dark matter targets and generate both heat and excited atoms during interactions.

- **Bubble chambers** utilize superheated liquids as target material. These liquids are maintained at a temperature just above their boiling point to facilitate a phase transition, creating a bubble whenever energy above a certain threshold is deposited.

- Lastly, **directional detectors** aim at determining the direction of the WIMP-induced nuclear recoil. Most of these detectors use low-pressure gas targets with photographic readout.

The above designs exhibit an assortment of strengths and weaknesses and, in many cases, emphasize different aspects of dark matter detection. They reflect the diverse and dynamic nature of the ongoing global effort to detect and understand dark matter. Direct detection experiments are notable for their ability to search for both nuclear and electron recoils, a feature that allows for a broader exploration of dark matter interactions [21]. However, these experiments face a significant challenge known as the "neutrino floor" or "neutrino fog," where neutrino interactions can mimic dark matter signals, complicating the detection process [48]. This necessitates innovative approaches in experiment design to differentiate between neutrino and potential dark matter interactions. The current state of spin-independent interactions between WIMP and nucleons is illustrated in figure 1.3. The toughest restrictions for a WIMP mass above roughly 3 $\mathrm{GeV/c^2}$ are imposed by LXe TPCs, including XENON1T, LUX, and PandaX-II. XENON1T outperforms others in this mass range, largely because of its substantial target mass and exposure. LAr experiments like DarkSide-50 and DEAP-3600 currently face constraints due to the need for significantly greater exposure than xenon and low acceptance in DEAP-3600.

1.3 Local dark matter distribution

The local dark matter distribution is critical for direct dark matter detection. The Standard Halo Model (SHM), which is the simplest model to describe the distribution and behavior of dark matter in galaxies, assumes that galaxies, including the Milky Way, are embedded in an isothermal dark matter halo, that is spherically symmetric with isotropic Maxwellain velocity distribution. The conventional value for local dark matter density, as per the SHM, is around $0.3\,\mathrm{GeV/cm^3}$, but estimates vary between 0.2 and $0.6\,\mathrm{GeV/cm^3}$ [36][51].

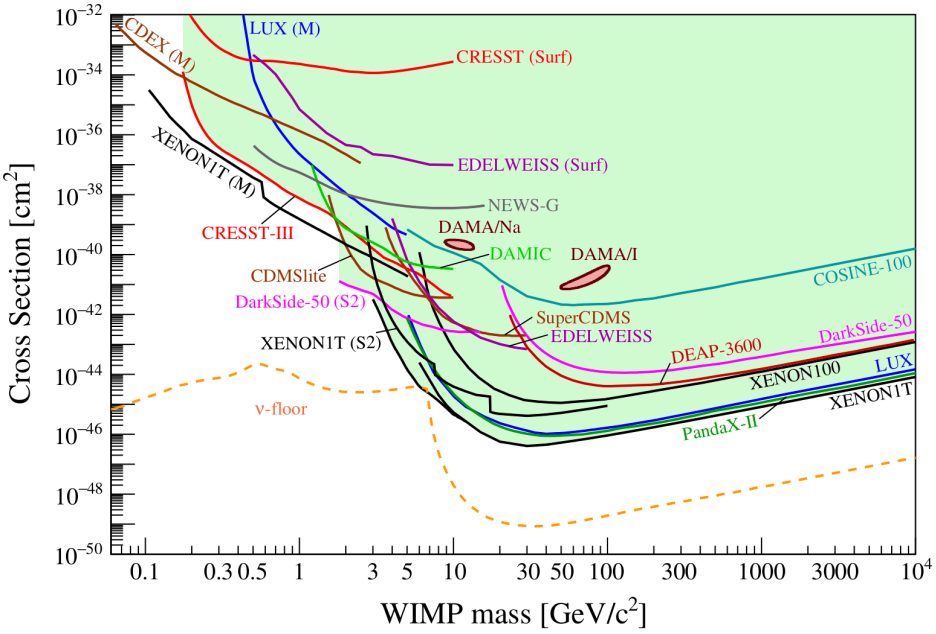

Figure 1.3: The recent state of inquiries into spin-independent elastic WIMP-nucleus scattering, under the assumption of standard isothermal WIMP halo parameters, namely: a local density of $\rho_\chi = 0.3\,\mathrm{GeV/cm^3}$, $v_0 = 220\,\mathrm{km/s}$, and $v_{esc} = 544\,\mathrm{km/s}$. (figure from ref. [13])

1.4 Cosmological and hydrodynamical simulations

The process of cosmic structure formation is exceptionally intricate, necessitating the use of both analytical models and numerical simulations for a comprehensive understanding.

Numerical simulations are crucial for accurately tracing the formation and evolution of cosmic structure, especially in the non-linear regime. Early cosmological simulations focused on gravitational interactions, treating particles as collisionless and not considering baryonic physics, known as N-body or dark matter only simulations. Prominent examples of dark matter only simulations include the Millennium-II simulation, which provides insights into dark matter statistics like halo mass function and subhalo abundance distribution [14], and the Aquarius project, known for its high-resolution simulations of dark matter halos and their role in galaxy formation [46][45]. These simulations have been instrumental in advancing our understanding of dark matter and

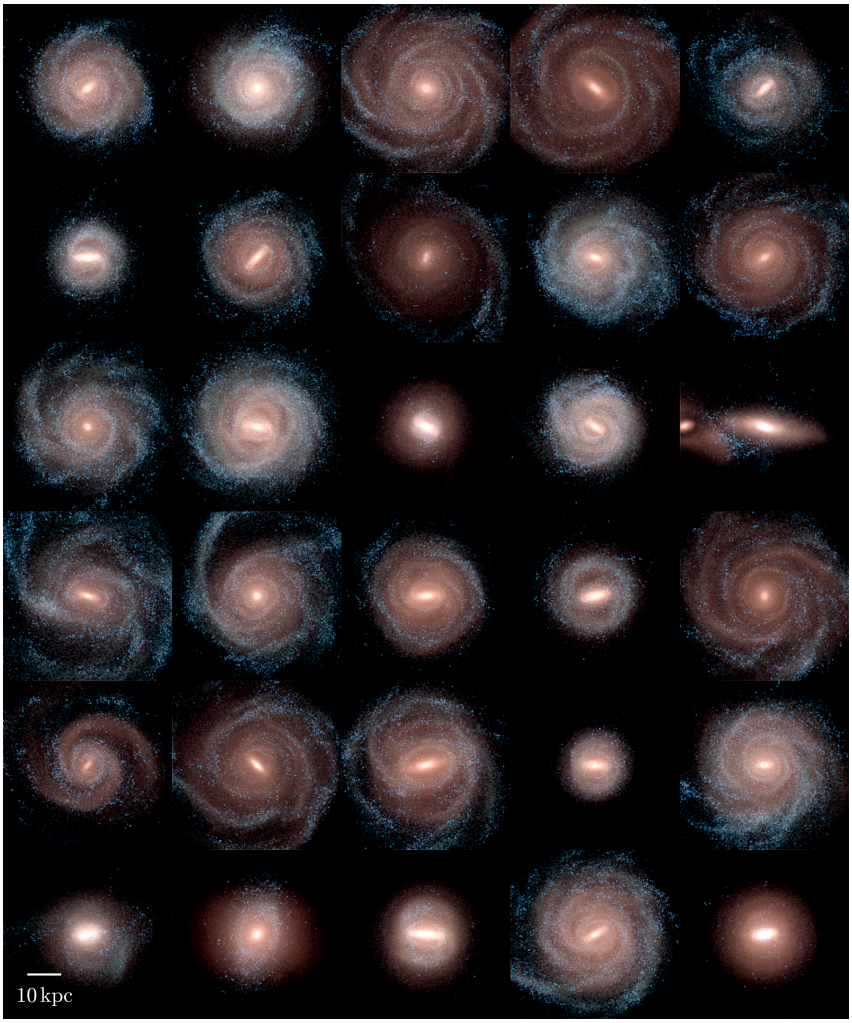

Figure 1.4: The face-on view of stellar densities of the 30 Auriga Mikly Way-mass halos at $z = 0$. (figure from ref. [35])

the large-scale structure of the universe. Advanced hydrodynamical simulations, despite being computationally expensive, offer a more comprehensive analysis by incorporating both dark and baryonic matter. These simulations include crucial processes like radiative heat loss and gas merging within halos, although they require subgrid models for finer details. Projects such as EAGLE [59], Illustris [65], and FIRE [38] have made significant strides in this area, closely mirroring observed galactic characteristics.

1.4.1 The Auriga simulation project

The Auriga project [35] represents a significant advancement in simulating Milky Way-like galaxies. Utilizing the Arepo code [62], Auriga integrates magnetohydrodynamics to explore the effects of magnetic fields on galaxy formation. The project includes 30 isolated Milky Way-mass halos, selected from a $100^3\,\mathrm{Mpc}^3$ periodic cube from the EAGLE project, using Planck-2015 [2] cosmological parameters. The dark matter particles in these simulations have a mass of about $3 \times 10^5\,\mathrm{M}_\odot$ with a Plummer equivalent gravitational softening of $\epsilon = 370\,\mathrm{pc}$ [39][52]. The Auriga simulations have been successful in replicating key features of current Milky Way-mass galaxies, such as stellar masses, rotation curves, and star formation rates (figure 1.4).

1.5 Influence of the Large Magellanic Cloud

Data from missions like Gaia [18] and the SDSS [66] have highlighted the presence of kinematic substructures within the Milky Way [49][47]. Moreover, recent hydrodynamic simulations have revealed that the LMC significantly influences the local dark matter distribution and the dark matter halo of the Milky Way. Studies have shown that the LMC affects the velocity distribution of dark matter in our Solar System [12][22].

Recent research [28][22] has delved into the influence of the LMC on the Milky Way's local dark matter composition and its dark matter halo. The study in ref. [28], utilizing idealized N-body simulations tailored for the Milky Way-LMC dynamics, uncovered that the LMC's gravitational influence considerably alters the orbits of native dark matter particles of the Milky Way, in addition to affecting the high speed tail of the dark matter velocity distribution in our Solar vicinity due to dark matter particles stemming from the LMC. Similarly, ref. [22] illustrated that the LMC's proximity during its pericenter passage augments the dark matter velocity distribution in the Solar region, with the dark matter particles of the Milky Way also getting a boost due to the LMC-induced reflex motion during its approach [32]. This aligns with the observations of ref. [28].

While the idealized simulations in references [28] and [22] align well with the LMC's orbit and characteristics within the Milky Way halo, it's still uncertain if such findings hold true for cosmological halos that have experienced numerous accretion episodes throughout their evolution. A pivotal inquiry revolves around whether a recent and proximate pericentric approach by a massive satellite, less than 100 Myr and within 100 kpc, can leave a notable imprint on the local dark matter distribution. Equally intriguing is the question of whether the increase in the local dark matter velocity distribution is a typical outcome across different Sun-LMC configurations, or if specific Sun-LMC geometries heighten the effect. Hence, cosmological simulations that sample potential Milky Way formation histories are essential to understanding the details of the Milky Way-LMC interaction and the variability in outcomes between different halos [56].

Understanding the influence of the LMC on our local dark matter distribution requires us to identify simulation-based LMC counterparts that mirror the observed LMC's properties. The LMC recently went through its first pericenter approach about 50 Myr ago [6]. As a result, we will use the LMC's properties at or shortly after this first pericenter approach. Current observational data indicates that the LMC's stellar mass is approximately $2.7 \times 10^9\,\mathrm{M}_\odot$ [44]. The LMC approached its first pericenter at roughly 48 kpc [6], with a speed relative to the Milky Way of $340 \pm 19\,\mathrm{km/s}$ [55]. Its current speed, when compared to the center of the Milky Way, is $321 \pm 24\,\mathrm{km/s}$ [42].

1.6 Outline of this thesis

The thesis is structured as follows: Chapter 2 outlines the methodology, including the specifics of the simulations, the criteria for selecting Milky Way-LMC analogues, and the process for determining the Sun's position within these simulations. This chapter lays the groundwork for understanding the intricate simulations used to model the Milky Way-LMC system and its interaction.

The thesis then progresses to a detailed analysis of the local dark matter density and velocity distributions, as presented in Chapter 3. This part of

the study highlights how the presence of the LMC alters these distributions, offering new insights into the dark matter structure within the Solar vicinity and its dynamic changes influenced by the LMC.

Chapter 4 is dedicated to the analysis of the halo integral, an essential component in dark matter direct detection computations. It emphasizes the impact of the LMC on the halo integral, particularly its influence on the high speed tails, which are critical for detecting low-mass dark matter particles.

In Chapter 5, the implications of the LMC's presence for dark matter direct detection signals are discussed. The chapter elaborates on both dark matter-nucleus and dark matter-electron scattering, exploring how the LMC's influence alters the expected signals in these detection methods. The focus is on the anticipated changes in the exclusion limits of forthcoming direct detection experiments due to the LMC's impact.

The thesis concludes in Chapter 6 with a summary of the key findings and their significance. It underscores the necessity of considering the LMC's role in future dark matter direct detection data analysis, especially for lower dark matter masses, thereby highlighting the study's contribution to understanding the nature of dark matter.

Chapter 2

Auriga simulation

In this study, the magneto-hydrodynamical simulations from the Auriga project are utilized to examine Milky Way mass halos. These simulations are conducted employing the moving-mesh code, Arepo, accompanied by a galaxy formation subgrid model. This model encompasses various processes such as metal cooling, formation of black holes, Active Galactic Nucleus (AGN) and supernova feedback, star formation, and background UV/X-ray photoionization radiation [35].

The cosmological parameters applied in these simulations align with Planck-2015 findings: $\Omega_m = 0.307$, $\Omega_{\rm bar} = 0.048$, $H_0 = 67.77$ km s^{-1} Mpc^{-1}. The selected resolution for these simulations is at Level 4, incorporating a dark matter particle mass ($m_{\rm DM}$) of approximately $3 \times 10^5\,{\rm M}_\odot$, a baryonic mass element (m_b) of $5 \times 10^4\,{\rm M}_\odot$. Notably, the simulations within the Auriga project have successfully reproduced the observed attributes of present day Milky Way-mass galaxies, such as stellar masses, sizes, rotation curves, star formation rates, and metallicities.

2.1 Selection criteria for Milky Way-LMC analogues

Given the vast array of possible Milky Way-LMC interactions, finding an exact analogue within cosmological simulations can be challenging. This task becomes even more daunting given our sample of just 30 Milky Way-mass halos. To enhance the probability of finding a match, we do not just focus

Halo ID	Auriga ID	$r_{\rm LMC}$ [kpc]	$t_{\rm LB}$ [Gyr]	$M_*^{\rm LMC}$ [10^9 M$_\odot$]	$M_*^{\rm MW}$ [10^{10} M$_\odot$]	$M_{200}^{\rm MW}$ [10^{12} M$_\odot$]
1	Au-1	53.1	5.1	0.66	1.5	0.40
2	Au-7	49.2	4.2	0.56	2.3	0.93
3	Au-12	49.4	4.6	0.79	3.3	1.1
4	Au-13	45.8	6.7	2.4	2.6	0.95
5	Au-13	56.7	7.4	3.1	1.6	0.72
6	Au-14	45.6	6.7	3.3	3.7	1.3
7	Au-14	49.9	2.3	0.99	9.3	1.6
8	Au-17	54.0	7.1	0.85	5.0	0.89
9	Au-19	40.9	6.2	1.6	1.8	0.66
10	Au-19	50.8	5.4	9.1	2.1	1.2
11	Au-21	55.5	3.3	4.8	6.7	1.7
12	Au-23	41.0	5.9	2.5	6.0	1.6
13	Au-25	43.2	1.0	15	3.7	1.2
14	Au-27	58.9	6.3	1.0	5.6	1.6
15	Au-30	56.0	6.3	2.5	7.3	0.97

Table 2.1: Characteristics of the 15 Milky Way-LMC candidates. Columns one and two provide the respective Halo ID and Auriga ID for each candidate. Columns three to seven offer details based on the simulation snapshot nearest to the LMC's first pericenter passage, detailing parameters such as the LMC counterpart's distance from its host ($r_{\rm LMC}$), the lookback duration ($t_{\rm LB}$), the Milky Way models' stellar and virial masses denoted by $M^*_{\rm MW}$ and $M^{200}_{\rm MW}$, and the stellar mass of the LMC candidates ($M^*_{\rm LMC}$). The final column provides information on the LMC's virial mass during its infall, represented by $M^{\rm Infall}_{\rm LMC}$. (table from ref. [60])

on the present but also trace back the history of these simulated Milky Way analogues, searching for any Milky Way-LMC similar interactions since redshift $z = 1$ (which equates to the past 8 billion years). Among the 30 Auriga halos, we select those that have an LMC analogue using two primary criteria: (i) the LMC counterpart's stellar mass should exceed $5 \times 10^8\,{\rm M}_\odot$, and (ii) its distance from its host during the first pericenter should be between [40-60] kpc. Based on these criteria, 15 Milky Way-LMC analogues are found, and we analyze them using the simulation data closest in time to the LMC's first pericenter approach. We treat this simulation snapshot as a representation of the current Milky Way-LMC scenario. It is worth noting, however, that with an average interval of roughly 150 Myr between these simulation snapshots, obtaining an exact "present day" snapshot for the 15 Milky Way-LMC analogues is challenging. This considerable gap in simulation data is a limitation we acknowledge and further explore below.

Table 2.1 provides a detailed breakdown of the properties of these 15 Milky

Way-LMC analogues. Beginning with the table's first two columns, they display the halo ID of the Milky Way-LMC counterparts and the corresponding Auriga ID for the Milky Way hosts of the LMC. Following that, the next five columns detail the characteristics of these counterparts during their closest snapshot to the LMC's first pericenter approach. These columns, from left to right, highlight: the distance of the LMC analogues from their hosts ($r_{\rm LMC}$), the lookback time ($t_{\rm LB}$), the Milky Way analogues' stellar mass ($M_*^{\rm MW}$), the Milky Way analogues' virial mass ($M_{200}^{\rm MW}$), and the LMC analogues' stellar mass ($M_*^{\rm LMC}$). The last column notes the LMC counterparts' virial mass at the time of their infall ($M_{\rm LMC}^{\rm Infall}$). The velocity of these LMC analogues relative to the center of their Milky Way counterparts ranges between [205 - 376] km/s during the snapshot closest to their first pericenter approach.

Based on our findings presented in table 2.1, it is evident that five of the LMC analogues we have identified possess a halo mass at infall, denoted as $M_{\rm LMC}^{\rm Infall}$, that is $\lesssim 0.4 \times 10^{11}\,{\rm M}_\odot$. Turning our attention to the actual LMC, its halo mass at the point of infall has been approximated to range around $[1-3] \times 10^{11}\,{\rm M}_\odot$, as cited in ref. [24].

An intriguing aspect to consider is the proportion between the LMC's halo mass at infall and the halo mass of the Milky Way. In our research, for five out of the Milky Way-LMC analogues, the ratio $M_{\rm LMC}^{\rm Infall}/M_{\rm MW}^{200}$ stands at $\lesssim 0.05$. This ratio is notably ~ 3 times lower than the mass ratio between the LMC and Milky Way as derived from observational data.

Such LMC analogues might exert a diminished overall influence on their respective host halos. Consequently, they might introduce fewer dark matter particles in the Sun neighborhood and induce a milder reflex motion in their Milky Way counterparts, as inferred from ref. [22].

However, a challenge arises when trying to compare the halo masses of these LMC analogues acquired through cosmological simulations against prior observation-based estimates. The latter often tends to consider a steady mass over time or sometimes just a singular point mass. Given these complexities, we opted to encompass the LMC analogues, even those with a diminished halo mass during infall, into our research to broaden the scope of our study.

Delving deeper into section 3.1, we illuminate on the potential consequences of the reduced LMC to Milky Way mass ratio, especially concerning the count of dark matter particles originating from the LMC in our immediate vicinity.

To gain deeper insight into the influence of the LMC on the local dark matter distribution during various stages of its orbit, we pinpoint one Milky Way-LMC analogue, specifically halo 13 which aligns with the Auriga 25 halo (referred to as Au-25) and its corresponding LMC satellite. Interestingly, this system includes the second massive LMC halo mass during its infall, almost reaching the peak estimated from empirical observations. As a result, its $M_{\rm LMC}^{\rm Infall}/M_{\rm MW}^{200}$ ratio stands at 0.27. We proceeded to conduct an enhanced simulation for halo 13, capturing more detailed snapshots around the time of LMC's pericenter. The span between these enhanced snapshots averages around 10 Myr.

Four crucial snapshots were selected for halo 13:

1. **Iso.**: This snapshot depicts the maximum separation between the Milky Way and LMC analogues, which is about 2.83 Gyr before the present day snapshot. This essentially serves as a benchmark for an isolated Milky Way.

2. **Peri.**: This snapshot represents the closest proximity (pericenter) of the LMC, which is roughly 133 Myr before the present day snapshot.

3. **Pres.**: This is essentially the snapshot most similar to the current separation seen between the real Milky Way and LMC systems.

4. **Fut.**: This serves as an anticipated projection of the Milky Way-LMC system, approximately 175 Myr post the present day snapshot.

Table 2.2 offers a summary of these four snapshots, indicating their temporal position with respect to the present day and the distance of the LMC analogue from its main host at each of these instances. For reference, the LMC model's distance and speed relative to its main host in the present day snapshot are about 50 kpc and 317 km/s, aligning strikingly well with observational measurements. The subsequent chapter will showcase broad findings

Snapshot	Description	$t - t_{\text{Pres.}}$ [Gyr]	r_{LMC} [kpc]
Iso.	Isolated Milky Way analogue	-2.83	384
Peri.	LMC's first pericenter approach	-0.133	32.9
Pres.	Present day Milky Way-LMC analogue	0	50.6
Fut.	Future Milky Way-LMC analogue	0.175	80.3

Table 2.2: Explanation of the four distinctive snapshots within halo 13, their respective timelines with respect to the present day snapshot, and the separation of the LMC analogue from its host during each snapshot. (table from ref. [60])

for the 15 picked Milky Way-LMC analogues at the snapshot that is closest to the LMC's first pericenter approach. Our primary emphasis, however, will be on halo 13, as we seek to understand the effects of the LMC's trajectory on the local dark matter distribution as it orbits around the Milky Way.

2.2 Matching the Sun-LMC geometry

The spatial configuration between the Sun and the LMC is uniquely structured, where the LMC primarily travels in a direction counter to the Solar motion. This distinctive orientation facilitates a significant increase in relative velocities of particles that originate from the LMC to the Sun, amplifying the dark matter velocity distribution near the Solar region [12]. Ref. [12] has highlighted the necessity of accurately replicating the real-world Sun-LMC geometry within simulations, emphasizing its critical role in precisely assessing the LMC's influence on the local dark matter distribution.

Accurately mimicking this geometry in simulations is pivotal for a nuanced understanding of the LMC's effect on local dark matter distribution patterns. The LMC influences the local Milky Way dark matter halo by directly contributing particles and accelerating them to speeds over 700 km/s relative to Earth, exceeding the velocities typically assumed in the SHM. The high speed particles' velocity vectors align with the LMC's motion at its closest approach, paralleling the Sun's reflex motion, and showing a concentrated spatial distribution skewed towards the South [26]. Furthermore, a radially biased initial velocity anisotropy profile in the Milky Way enhances the LMC's acceleration

effect on Milky Way dark matter particles.

In the conducted simulations, the Sun's position is undetermined beforehand, and the LMC analogues exhibit phase-space coordinates that diverge from the actual Milky Way-LMC system. This necessitates the selection of a Sun position within each Milky Way analogue, driven by specific criteria aimed at aligning with the observed Sun-LMC geometry. The criticality of precisely matching the Sun-LMC geometry in the simulations to significantly influence the local dark matter velocity distribution is also a subject of exploration in this study.

Our initial focus is on explaining the methodology employed to ascertain all allowed Sun positions in the simulations, aligning closely with the observed Sun-LMC geometry. Following this, the discourse evolves toward defining the "best fit" position of the Sun within the simulations, a position that resonates most accurately with the observed geometric configuration of the Sun-LMC. Through this approach, the study aims to discover the positions that most effectively match the observed Sun-LMC relative geometry.

Figure 2.1 illustrates the geometrical arrangement of the Sun-LMC system within a defined Galactocentric reference frame. The origin of this frame is at the Galactic center. The coordinate axes x_g and y_g are strategically aligned with the orbital plane of the Sun, with the x_g-axis oriented towards the Galactic center originating from the Sun, and the y_g-axis aligning with the direction of Galactic rotation. The z_g-axis, conversely, points towards the North Galactic Pole. The diagram specifically outlines various directional components such as the Sun's position ($\mathbf{r}_{\rm Sun}$), the velocity of the Sun ($\mathbf{v}_{\rm Sun}$), as well as the position ($\mathbf{r}_{\rm LMC}$) and velocity ($\mathbf{v}_{\rm LMC}$) of the LMC. Additionally, it also illustrates the orbital angular momentum of the LMC ($\mathbf{L}_{\rm LMC}$).

In our simulations, the core of the Milky Way and LMC analogues is determined by the location of the particle—whether star, gas, dark matter, or black hole—that holds the minimum gravitational potential energy in each halo. The center of mass velocity of all particles bound to each halo, determined using the SUBFIND algorithm [63], signifies the velocity of the Milky Way and LMC analogues within the simulation reference frame. Subsequently,

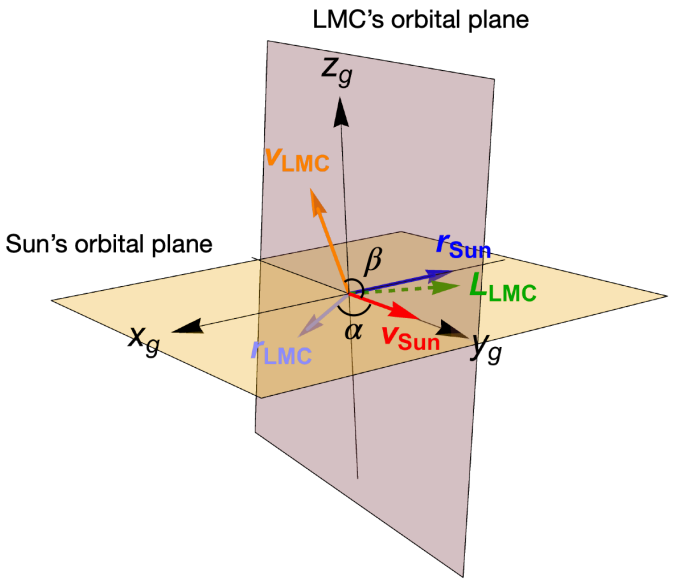

Figure 2.1: The diagram presents a detailed visualization of the Sun-LMC geometry as observed. Blue and red vectors represent the Sun's position ($\mathbf{r}_{\rm Sun}$) and velocity ($\mathbf{v}_{\rm Sun}$), respectively. Concurrently, the position ($\mathbf{r}_{\rm LMC}$) and velocity ($\mathbf{v}_{\rm LMC}$) of the LMC are depicted by light blue and orange vectors. Angles within the system are also highlighted; angle α represents the angle between $\mathbf{r}_{\rm LMC}$ and $\mathbf{v}_{\rm Sun}$, and angle β is defined between $\mathbf{v}_{\rm LMC}$ and $\mathbf{v}_{\rm Sun}$. A dashed green vector is used to illustrate the LMC's orbital angular momentum direction ($\mathbf{L}_{\rm LMC}$). The diagram also displays the orbital planes of both the Sun and the LMC, indicating that they are almost perpendicular to each other. (figure from ref. [60])

the LMC analogue's position and velocity are discerned relative to the Milky Way analogue's center.

Our approach to aligning the simulated Sun-LMC geometry with the observed geometry involves a specific methodology. Initially, we adopt stellar disk orientations that maintain a constant angular momentum angle between the stellar disk and the LMC analogue's orbital angular momentum, $\mathbf{L}^{\rm sim}_{\rm LMC}$, consistent with the observed Milky Way-LMC pair. Various allowed orientations for the stellar disk of the simulated Milky Way analogue emerge from this criterion, as illustrated in figure 2.1.

In further steps, the Sun's position relative to the Milky Way analogue's center is identified for each permissible disk orientation, ensuring the angular alignments concerning the LMC's orbital angular momentum align closely with

observed values. This process results in the acquisition of multiple allowed Sun positions for each halo due to the variety of allowable disk orientations. Chapter 4 will explore the variances in Milky Way-LMC interaction signatures attributable to these different Sun positions.

Furthermore, we engage in identifying the best fit position for the Sun. Figure 2.1 illustrates that the Sun's position vector primarily aligns with the LMC's angular momentum direction, exhibiting minimal variation across different disk orientations. However, a broader spectrum of variations is observed in the Sun's velocity vector, necessitating a more refined alignment with observational data. To facilitate this, we introduce the cosine angles,

$$\begin{aligned} \cos\alpha &\equiv \hat{\mathbf{v}}^{\rm sim}_{\rm Sun} \cdot \hat{\mathbf{r}}^{\rm sim}_{\rm LMC} \,, \\ \cos\beta &\equiv \hat{\mathbf{v}}^{\rm sim}_{\rm Sun} \cdot \hat{\mathbf{v}}^{\rm sim}_{\rm LMC} \,, \end{aligned} \tag{2.1}$$

where the simulated Sun's velocity vector, denoted as $\hat{\mathbf{v}}^{\rm sim}_{\rm Sun}$, is aligned with the Sun's velocity relative to the Milky Way analogue's center. Similarly, the simulated LMC's position and velocity vectors, $\hat{\mathbf{r}}^{\rm sim}_{\rm LMC}$ and $\hat{\mathbf{v}}^{\rm sim}_{\rm LMC}$ respectively, correspond to their directions relative to the Milky Way analogue's center.

To find the best fit, the final step involves selecting an orientation that closely aligns with the observed cosine angles:

$$\begin{aligned} \hat{\mathbf{v}}^{\rm obs}_{\rm Sun} \cdot \hat{\mathbf{r}}^{\rm obs}_{\rm LMC} &= -0.835 \,, \\ \hat{\mathbf{v}}^{\rm obs}_{\rm Sun} \cdot \hat{\mathbf{v}}^{\rm obs}_{\rm LMC} &= -0.709 \,. \end{aligned} \tag{2.2}$$

To determine the most accurate Sun's position in the simulations, the focus is on minimizing the sum of squared differences between the simulated and observed values of $\cos\alpha$ and $\cos\beta$. This process, anchored by the observational data in eq. (2.2), pinpoints the best fit Sun-LMC geometry in the simulations.

Prior research utilizing EAGLE and APOSTLE simulations suggests a minimal influence of the stellar disk on the local dark matter velocity distribution [15][58]. Contrastingly, specific studies [22][58] indicate that the stellar disk's presence and its non-axisymmetric evolution could boost the local dark matter velocity distribution. It is noteworthy that some Auriga halos display

a minor dark matter component aligned with the stellar disk's rotation due to accretion occurrences [33], although these halos are excluded from our Milky Way-LMC analogue sample.

Chapter 3

Local dark matter distribution

In our study, we critically examine how different assumptions about the dark matter distribution in the Solar neighborhood influence calculations of dark matter direct detection event rates. This analysis involves evaluating the dark matter density and velocity distribution in this region, derived from simulated Milky Way-LMC analogues. A significant aspect of our investigation is understanding the impact of the LMC on these parameters.

The process for determining the Solar neighborhood's dark matter characteristics starts by establishing the Galactic reference frame (x_g, y_g, z_g), as outlined in section 2.2. This frame is oriented based on each allowed position and velocity of the Sun that aligns with the observed Sun-LMC geometry. Subsequently, we convert the simulation particles' positions and velocities to this Galactic frame.

To precisely define the Solar neighborhood, we initially focus on a spherical shell, positioned at a galactocentric distance of approximately 8 kpc from the center of the Milky Way analogue. This shell's radius spans between 6 to 10 kpc. Further refinement involves considering a cone with an opening angle of $\pi/4$ radians, originating at the Galactic center and aligned along the Sun's position derived earlier. The overlap of this cone with the spherical shell forms what we designate as the Solar region, depicted as the shaded blue area in figure 3.1.

The dimensions of the Solar region are carefully chosen: large enough to encompass several thousand dark matter particles, yet sufficiently small to

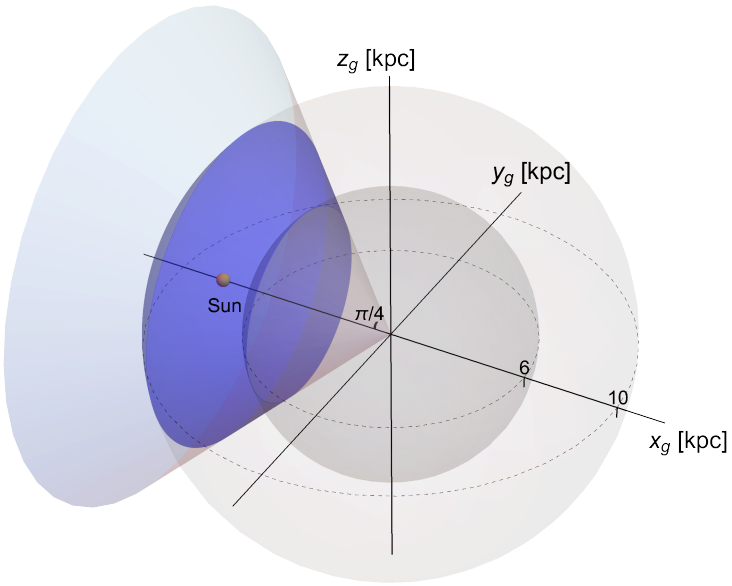

Figure 3.1: In this figure, we focus on a specific region in the Solar neighbourhood, depicted in blue. This area represents the intersection of two distinct volumes: one is a cone originating from the Galactic center, having an opening angle of $\pi/4$ radians, with its axis aligned to the Sun's position; the other is the space bounded by two spheres centered at the Galactic center, with radii of 6 and 10 kpc, respectively. For clarity in this depiction, the Sun is positioned on the axis of the cone, located at a distance of 8 kpc from the Galactic center. (figure from ref. [60])

maintain a high sensitivity to the best fit Sun's position. In sections 3.1 and 4.4, we study how alterations in the Solar region's size affect various parameters. These include the local dark matter density, the proportion of dark matter particles in the Solar neighborhood originating from the LMC, and the halo integrals.

The procedure outlined earlier results in varying Sun positions for each Milky Way analogue and snapshot, leading to different Solar regions for each case. Table 3.1 lists the counts of native dark matter particles in the Milky Way (N_{MW}) and those originating from the LMC (N_{LMC}) within the Solar neighborhood, specifically for the snapshot nearest to the LMC's first pericenter approach across the 15 Milky Way-LMC analogues. The count of Milky Way's dark matter particles in this region ranges from $7,760$ to $20,001$, while the LMC-derived dark matter particles vary from 1 to 361.

Halo ID	$N_{\rm MW}$	$N_{\rm LMC}$	ρ_χ [GeV/cm^3]	$\kappa_{\rm LMC}$ [%]	$\kappa_{\rm LMC}$ Range [%]	$v_{\rm esc}^{\rm det}$ [km/s]
1	7,760	11	0.21	0.14	$[0.14 - 0.21]$	651
2	8,581	55	0.23	0.64	$[0.53 - 0.65]$	720
3	11,621	3	0.35	0.026	$[0.025 - 0.028]$	714
4	12,483	12	0.34	0.096	$[0.088 - 0.12]$	737
5	8,669	136	0.24	1.5	$[1.4 - 1.6]$	707
6	13,290	5	0.38	0.038	$[0.029 - 0.046]$	734
7	18,467	6	0.53	0.032	$[0.032 - 0.034]$	766
8	12,949	1	0.38	0.0077	$[0.0077 - 0.0082]$	712
9	11,892	12	0.36	0.10	$[0.069 - 0.13]$	715
10	12,405	361	0.39	2.8	$[2.8 - 3.1]$	791
11	14,132	4	0.43	0.028	$[0.021 - 0.039]$	758
12	16,427	28	0.53	0.17	$[0.17 - 0.21]$	783
13	10,814	254	0.34	2.3	$[2.3 - 3.0]$	831
14	20,001	52	0.60	0.26	$[0.26 - 0.31]$	776
15	10,641	128	0.32	1.2	$[0.81 - 1.3]$	819

Table 3.1: In the Solar region, focusing on 15 Milky Way-LMC analogues, we examine several key parameters at the simulation snapshot that is closest to the LMC's pericenter. These parameters include: the halo ID, the count of native dark matter particles in the Milky Way denoted as $N_{\rm MW}$, the number of dark matter particles originating from the LMC $N_{\rm LMC}$, the local dark matter density ρ_χ, and the percentage of dark matter particles from the LMC in the Solar neighborhood $\kappa_{\rm LMC}$. This analysis also covers the range of possible values for $\kappa_{\rm LMC}$ considering various allowed positions of the Sun, and the local escape velocity from the Milky Way in the detector's rest frame $v_{\rm esc}^{\rm det}$. Except for the 6th column, all other columns present data based on the best fit Sun's position. (table from ref. [60])

This relatively small number of LMC particles in the Solar region implies a limited sensitivity to their distribution changes within this region. Despite this constraint, the high relative velocities of the LMC's dark matter particles relative to the Sun make them more abundant in the high speed range of the local dark matter velocity distribution than the Milky Way's high speed dark matter particles. This aspect means the low N_{LMC} figure does not significantly undermine our findings. However, the paucity of LMC-origin dark matter particles is a limitation of current cosmological simulations when compared to idealized simulations, which can offer finer resolution.

3.1 Dark matter density in the Auriga simulation

We commence by finding the local dark matter density, denoted as ρ_χ, specifically within the Solar neighborhood, using the best Sun's position fit. This analysis is carried out for a set of 15 Milky Way-LMC analogue systems within the Auriga simulation, considering the closest snapshot to the LMC's first pericenter approach. The outcomes of this analysis are presented in table 3.1. The range of local dark matter density is found to span from 0.21 to 0.60 $\mathrm{GeV/cm^3}$. This outcome concurs with earlier findings of the dark matter density in Milky Way-like halos, as observed in the EAGLE, APOSTLE [15], and Auriga [16] simulations. Moreover, it aligns favorably with both local and global estimates obtained from observational studies. Notably, the substantial variation in local dark matter densities across simulations can be attributed to variations among halos, contingent upon factors such as mass (with our simulated halos falling within a factor of 2 of the estimated Milky Way halo mass [19]), concentration, formation history, and the mass of the stellar disk.

Subsequently, we turn our attention to ascertaining the percentage of dark matter particles present in the Solar region that originate from the LMC analogue, κ_{LMC}. This analysis is performed at the snapshot closest to the LMC's initial pericenter approach. A dark matter particle is considered to have originated from the LMC analogue if it was gravitationally bound to the LMC at the time of infall, as identified by the SUBFIND algorithm, and its distance from the center of the LMC at infall is less than twice the virial radius of the LMC at that time. κ_{LMC} is formally defined as the ratio of the number of dark matter particles originating from the LMC analogue within the Solar region to the total number of dark matter particles present in the Solar region. This ratio is then multiplied by 100 to yield the percentage representation. For the 15 Milky Way-LMC analogue systems, the calculated values of κ_{LMC} within the Solar region, based on the best fit Sun's position, exhibit a range from 0.0077% to 2.8%, as delineated in Table 3.1. Additionally, the fourth column of the table provides the variability in κ_{LMC} for each halo, attributable to the

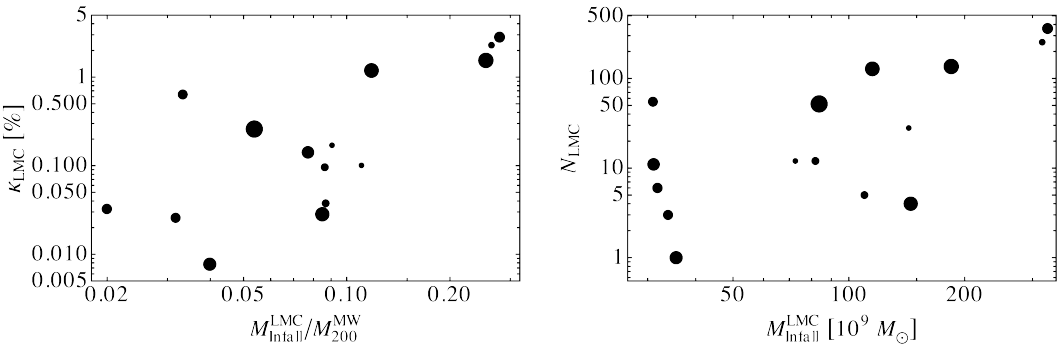

Figure 3.2: For the 15 Milky Way-LMC analogues, the relationship is examined between $\kappa_{\rm LMC}$ and the ratio $M_{\rm Infall}^{\rm LMC}/M_{200}^{\rm MW}$ (on the left side), and between $N_{\rm LMC}$ and $M_{\rm Infall}^{\rm LMC}$ (on the right side). In this analysis, $\kappa_{\rm LMC}$ and $N_{\rm LMC}$ values are specifically determined for the Solar region, based on the best fit Sun's position at the simulation snapshot which aligns closest to the LMC's approach to its pericenter. Additionally, the point sizes in these representations are scaled to correspond with the distance of LMC analogues to their host at the pericenter. (figure from ref. [60])

different permissible Sun's positions considered in the analysis.

To elucidate the underlying causes behind the variations observed in $\kappa_{\rm LMC}$ and $\rm N_{LMC}$ across different halos, we illustrate these parameter variations in figure 3.2. Specifically, we examine how these parameters change concerning the ratio of $M_{\rm Infall}^{\rm LMC}/M_{200}^{\rm MW}$ and $M_{\rm Infall}^{\rm LMC}$.

In figure 3.2, we depict the point sizes, which increase as the LMC analogues' distance from the host at pericenter grows. In the left panel, a general trend emerges, indicating that systems with a higher LMC to Milky Way halo mass ratio tend to have a larger proportion of LMC particles within the Solar region in most instances. However, it is important to note that these two parameters are not strongly correlated. In particular, systems with similar values of $M_{\rm Infall}^{\rm LMC}/M_{200}^{\rm MW}$ can still exhibit considerable variability in $\kappa_{\rm LMC}$. This variability primarily stems from differences in the distance of the LMC analogues from the host at the pericenter, $\rm r_{LMC}$. Larger values of $\rm r_{LMC}$ correspond to smaller $\kappa_{\rm LMC}$ values for systems with similar LMC to Milky Way mass ratios. Similarly, the right panel of the figure reveals a degree of correlation between $N_{\rm LMC}$ and $M_{\rm Infall}^{\rm LMC}$, while an inverse correlation exists between $N_{\rm LMC}$ and $\rm r_{LMC}$ for systems with similar $M_{\rm Infall}^{\rm LMC}$.

We have also investigated the impact of altering the size of our defined Solar region on ρ_χ and $\kappa_{\rm LMC}$. Specifically, for the re-simulated halo 13 at the present day snapshot, reducing the opening angle of the cone from $\pi/4$ to $\pi/6$ while keeping the spherical shell width constant results in a 50% reduction in both $N_{\rm LMC}$ and $N_{\rm MW}$, a $\sim 30\%$ decrease in ρ_χ, and a $\sim 20\%$ increase in $\kappa_{\rm LMC}$ compared to the original Solar region. Similarly, reducing the shell width from 6-10 kpc to 7-9 kpc while maintaining the cone's opening angle has a similar impact on $N_{\rm LMC}$ and $N_{\rm MW}$ but leads to a $\sim 2\%$ increase in ρ_χ and a $\sim 10\%$ increase in $\kappa_{\rm LMC}$.

Further, when both the cone's opening angle is reduced to $\pi/6$ and the shell width to 7-9 kpc, $\rm N_{LMC}$ drops to 1/3 and $\rm N_{MW}$ to 1/4 of their original values, ρ_χ decreases by $\sim 25\%$, and $\kappa_{\rm LMC}$ increases by $\sim 35\%$. Notably, these changes are comparatively smaller than the halo-to-halo variations in these parameters, as demonstrated in table 3.1.

3.2 Velocity distribution in the Auriga simulation

We will now proceed to determine the velocity distribution of dark matter in the Solar neighborhood, referencing the Galactic frame. The velocity vectors of dark matter particles in each halo are defined relative to the center of that halo. The dark matter speed distribution, denoted as $f(v)$, is described by

$$f(v) = v^2 \int d\Omega_{\mathbf{v}} \tilde{f}(\mathbf{v}) \ . \tag{3.1}$$

where $d\Omega_{\mathbf{v}}$ is an infinitesimal solid angle in direction $\mathbf{v}$, and $\tilde{f}(\mathbf{v})$ is the normalized dark matter velocity distribution, ensuring that $\int dv f(v) = \int d^3v \tilde{f}(\mathbf{v})$ equals 1.

In the SHM, the local circular speed of the Milky Way is often assumed to be 220 km/s. For cross-halo comparison of local dark matter speed distributions, we adjust the dark matter speeds in the Solar region by the ratio (220 km/s)/v_c. Here, v_c represents the local circular speed determined by the total mass within a radius of 8 kpc in each halo. A speed bin size of 25 km/s

is selected for computing these distributions from the simulations, balancing the need for sufficient particles in each bin to minimize statistical noise and preserving potential characteristics in the dark matter speed distributions.

Figure 3.3 illustrates the dark matter speed distributions in the Galactic rest frame for four Milky Way-LMC analogue systems in the Solar neighborhood, based on their best fit positions for the Sun. This is specifically for the snapshot closest to the LMC's pericenter approach. The total dark matter particles' speed distribution (whether native to the Milky Way or from the LMC) in the Solar region is depicted as black shaded bands, indicating 1σ Poisson errors. In contrast, the red color represents the distribution of dark matter particles native to the Milky Way. The speed distributions of dark matter particles from the LMC, reduced by a factor of 10 for clarity, are shown in blue. Both the total and Milky Way-native dark matter particles' speed distributions are normalized to 1. Each panel's top left corner also indicates the percentage of dark matter particles in the Solar neighborhood that originated from the LMC. Panels beneath these distribution plots display the ratio of the total dark matter particles' speed distribution to that of the Milky Way-only.

The selected four halos from a pool of 15 Milky Way-LMC analogues, serve as examples highlighting the variance in local speed distributions of dark matter particles. For instance, Halo 2, shown in the top left of the figure, exhibits a remarkable characteristic: approximately 0.64% of its dark matter particles in the Solar neighborhood trace back to the LMC ($\kappa_{\rm LMC} = 0.64\%$). This halo is also characterized by a sharply peaked speed distribution. This results in pronounced disparities between the tails of the combined Milky Way+LMC and the Milky Way-only speed distributions. In these tails, the ratio of the two distributions exceeds 2.

Conversely, Halo 6, shown in the top right, demonstrates that even a minimal LMC-originating dark matter particle fraction in the Solar neighborhood ($\kappa_{\rm LMC} = 0.038\%$) can significantly affect the dark matter speed distribution tail, as evidenced in the corresponding ratio plot. Halo 13, depicted in the bottom left, is notable for its high LMC particle fraction ($\kappa_{\rm LMC} = 2.3\%$) and broad speed distribution, causing mild variations across a wide speed range

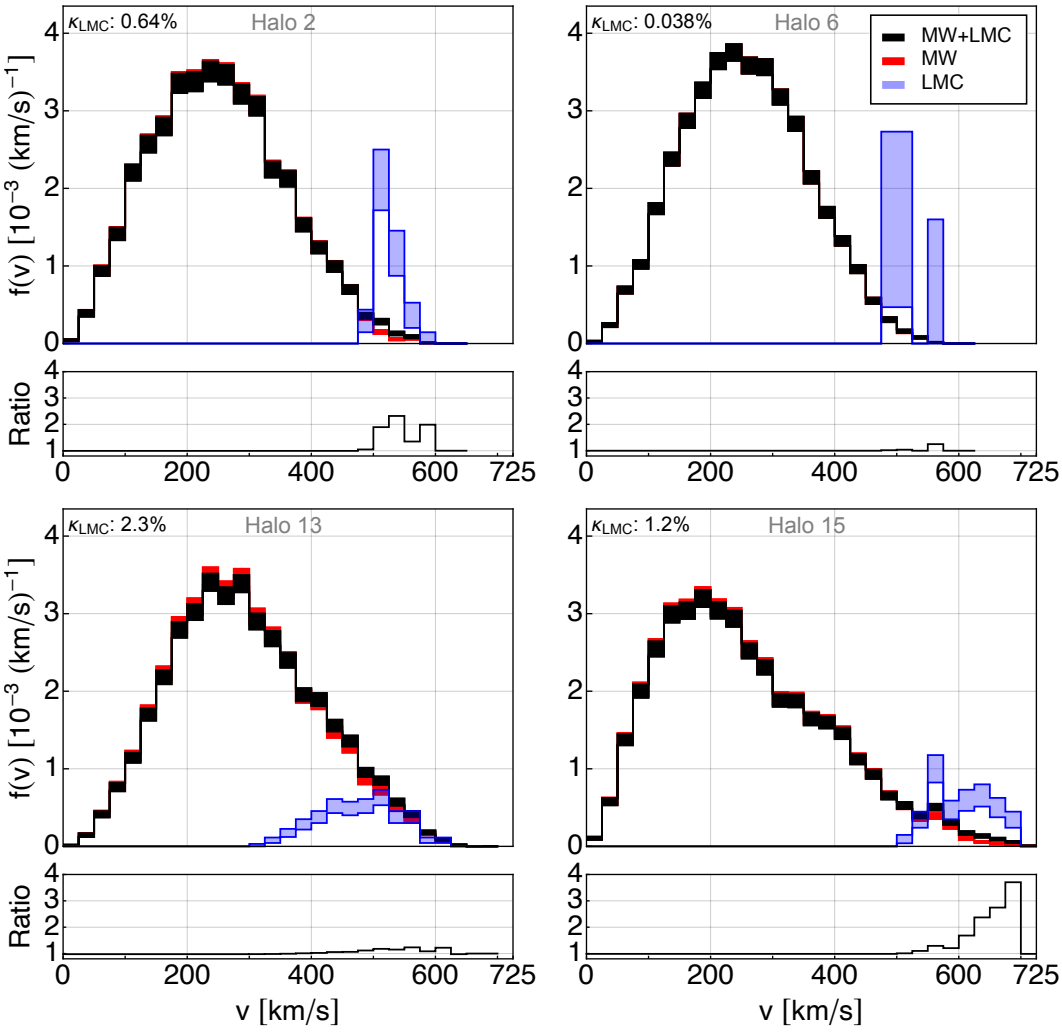

Figure 3.3: The speed distributions of dark matter in the Solar neighborhood and Galactic rest frame, specifically for the snapshot nearest to the LMC pericenter approach, across four Milky Way-LMC analogues: halos 2, 6, 13, and 15. These are represented in respective panels: top left, top right, bottom left, and bottom right, each based on the best fit for the Sun's position. The study delineates the distributions of dark matter particles from the combined Milky Way+LMC, Milky Way-only, and LMC-only, shown as black, red, and blue shaded bands that indicate the 1σ Poisson errors. For enhanced visualization, the LMC-only distribution is scaled down by a factor of 10. Each panel also includes the percentage of dark matter particles from the LMC in the Solar region, denoted as $\kappa_{\rm LMC}$. Additionally, the panels below the main plots compare the ratio between the combined Milky Way+LMC and the Milky Way-only distributions. (figure from ref. [60])

between the Milky Way+LMC and Milky Way-only speed distributions. Notably, Halos 6 and 13, despite the vast difference in their $\kappa_{\rm LMC}$ values (the

latter being about 60 times larger), reach similar ratio values in their distributions. Halo 15, located in the bottom right, with a $\kappa_{\rm LMC}$ of 1.2%, showcases significant divergence in the high speed tail between the Milky Way+LMC and Milky Way-only speed distributions, with their ratio nearing 4.

The dark matter particles from the LMC typically peak at higher speeds (exceeding 500 km/s relative to the Galactic center) compared to those from the Milky Way. This results in noticeable variations in the tail of the combined Milky Way+LMC speed distribution compared to the Milky Way-only distribution. However, the extent of these variations is highly variable across different halos. The specific characteristics of the LMC's speed distribution in the Solar neighborhood for each Milky Way analogue, such as its shape and width, play a crucial role in these variations. Interestingly, halos with even higher $\kappa_{\rm LMC}$ values, as listed in table 3.1, do not always exhibit substantial differences in their speed distributions ($f(v)$) with or without LMC particles.

In a deeper exploration of the LMC's influence on local dark matter distribution during its orbit, our focus shifts to Halo 13. We have re-run simulations with finer time steps around the LMC's pericenter approach. Figure 3.4 presents the local dark matter speed distributions for Halo 13 in the Galactic rest frame. These distributions are captured at four different stages of the LMC's orbit around the Milky Way analogue, as specified in table 2.2. Displayed are the speed distributions of dark matter particles exclusively from the Milky Way (red), solely from the LMC (blue), and the combined Milky Way+LMC (black) within the Solar region. The best fit Sun's position is used for these snapshots, with the exception of the isolated Milky Way snapshot, where no LMC analogue exists and thus the dark matter distribution is derived from a spherical shell 6 to 10 kpc from the Galactic center. Each panel includes the according $\kappa_{\rm LMC}$, and below the speed distribution plots, the ratio of the Milky Way+LMC to Milky Way-only distributions is shown for all snapshots except the isolated Milky Way.

Figure 3.4 reveals the influence of the LMC on the high speed tail of the local dark matter speed distribution. This impact is evident at three distinct timeframes: during the LMC's closest approach to the Milky Way, the present

day, and approximately 175 Myr thereafter. The parameter $\kappa_{\rm LMC}$, indicative of the LMC's effect, is found to be maximal at the LMC's pericenter, diminishing as it distances itself from the Milky Way. Concurrently, the comparative analysis of the high speed tail between combined Milky Way+LMC and Milky Way-only dark matter speed distributions mirrors this trend, showing a pronounced difference at pericenter which lessens in the present and future scenarios. Excluding the isolated Milky Way (where $\kappa_{\rm LMC} = 0$) snapshot, the LMC-derived dark matter displays a distinct speed distribution peaking at the higher end of the Milky Way's native dark matter speed distribution, imparting a subtle but significant influence on the overall dark matter speed distribution. This aligns with findings from 15 analogous Milky Way-LMC systems at pericenter, as depicted in figure 3.3.

When examining halo 13 through a lens of enhanced resolution, discrepancies emerge in the phase-space distribution of dark matter particles compared to the original simulation. This divergence is partly due to the non-identical temporal frames of the two simulations, where the average inter-snapshot time interval is about 150 Myr in the original simulation. Precisely capturing the present day or the LMC's pericenter becomes challenging under these circumstances. Additionally, the positional variances of the Sun in the original and refined simulations of halo 13 markedly affect the local dark matter velocity distribution. In the original simulation, the best fit Sun's position is defined by cosine angles (eq. 2.1) $\cos\alpha = -0.796$ and $\cos\beta = -0.090$, which, despite minimizing squared differences from observed values, exhibit notable discrepancies, particularly for $\cos\beta$ (refer to eq. (2.2)). In contrast, the refined simulation of halo 13 aligns more closely with the observed Sun position, for example, $\cos\alpha = -0.995$ and $\cos\beta = -0.656$ at the best fit position for the present day snapshot. This improved alignment leads to a higher speed peak for LMC-originating dark matter particles in the Solar region in the re-simulated halo compared to the original. Lastly, potential variations in the phase-space distribution could stem from the stochastic nature of the baryonic physics model, possibly altering the gravitational potential's evolution in the re-simulated halo. As a consequence, discrepancies arise in both the local dark

matter velocity distributions and the κ_{LMC} values between figures 3.3 and 3.4 for halo 13.

Our findings largely align with those in refs. [22] and [12], demonstrating that a minor percentage of dark matter particles from the LMC, such as approximately 0.2% as indicated in ref. [12], significantly influences the high-speed range of the local dark matter speed distribution. This conclusion is drawn from a series of idealized simulations. However, it is crucial to acknowledge the significant impact of variations between different halos, as observed in our cosmological simulations.

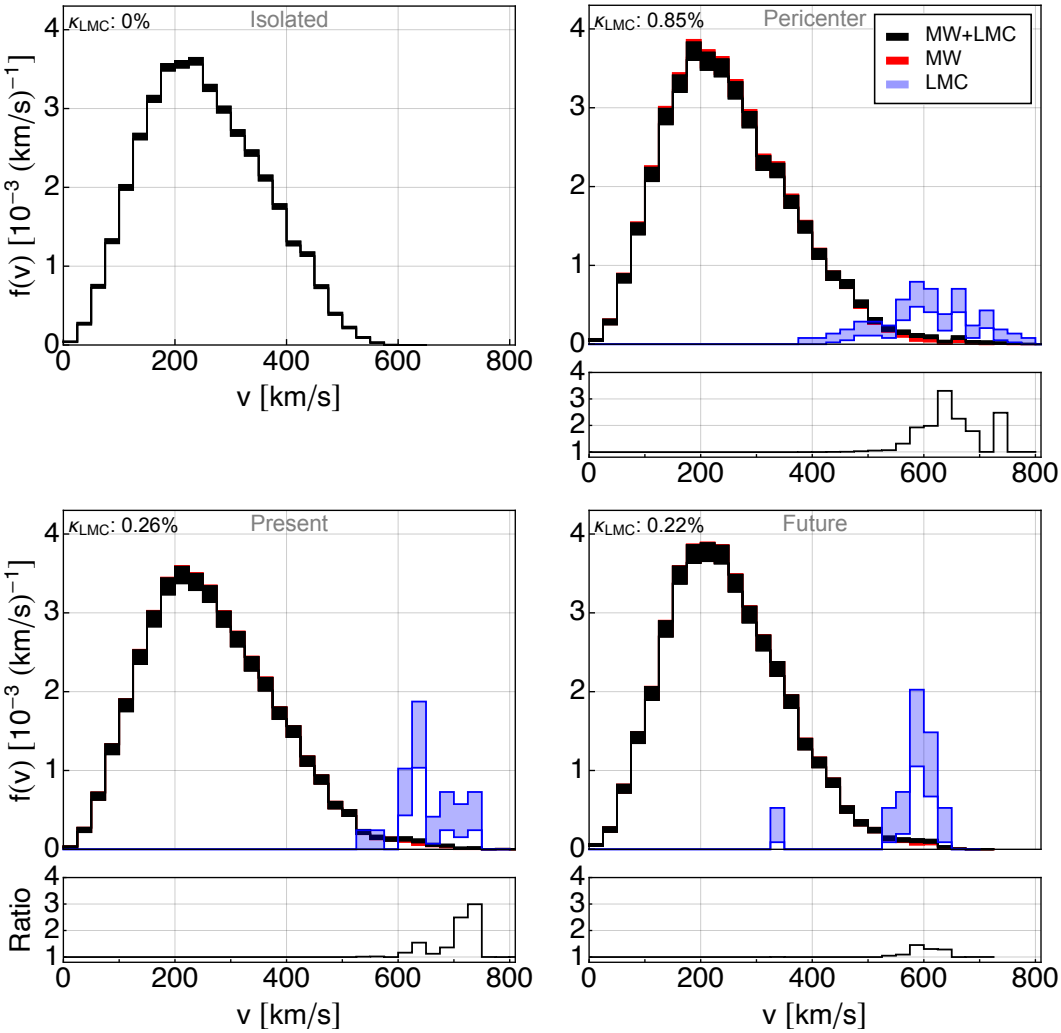

Figure 3.4: The speed distributions of dark matter in the Galactic rest frame, focusing on halo 13 during four key snapshots: the isolated Milky Way (top left), the LMC's pericenter (top right), the present day Milky Way-LMC configuration (bottom left), and a projected future state of Milky Way-LMC (bottom right). These distributions are showcased for the dark matter particles belonging to the combined Milky Way+LMC system, the Milky Way-only, and the LMC-only, depicted in black, red, and blue, respectively. Each distribution is accompanied by shaded bands indicating the 1σ Poisson errors. Notably, the LMC-only distribution is reduced by a factor of 10 for scaling purposes. For all snapshots except the isolated Milky Way, the distributions are analyzed in the Solar region, aligning with the best fit position of the Sun. In contrast, the isolated Milky Way's distribution is derived from a spherical shell, specifically between 6 and 10 kpc from the Galactic center. Each panel's top left corner highlights the value of $\kappa_{\rm LMC}$. The lower panels of each figure contrast the ratio of the combined Milky Way+LMC distribution to that of the Milky Way-only, excluding the isolated Milky Way snapshot. (figure from ref. [60])

Chapter 4

Halo integrals

In direct detection experiments, the event rate's astrophysical dependence is determined by the density and velocity distribution of dark matter in the vicinity of the Solar System. Specifically, when considering standard interactions, the event rate's reliance on the local dark matter velocity distribution is encapsulated within the halo integral. This integral is formulated as follows:

$$\eta(v_{\min}, t) \equiv \int_{v>v_{\min}} d^3v \, \frac{\tilde{f}_{\rm det}(\mathbf{v}, t)}{v} \, , \tag{4.1}$$

where $\mathbf{v}$ represents the relative velocity between the dark matter particle and the target nucleus or electron within the detector ($v = |\mathbf{v}|$). The local dark matter velocity distribution in the detector's frame of reference is denoted as $\tilde{f}_{\rm det}(\mathbf{v}, t)$. Additionally, $v_{\min}$ symbolizes the minimum velocity that a dark matter particle must possess to transfer sufficient energy and momentum for detection, resulting in recoil. This is further elaborated in equations (5.2) and (5.6), which delineate the criteria for nuclear and electron recoils, respectively. Understanding how the LMC affects these halo integrals, particularly in the Solar region, is crucial as it correlates directly with anticipated variations in the rates of direct detection events.

4.1 Velocity distribution transformation

In order to study the event rates in direct detection experiments, the dark matter velocity w.r.t. the detector should be calculated. By implementing a Galilean boost, we adjust the galactic frame velocity distribution, represented

as $\tilde{f}_{\rm gal}(\mathbf{v})$,

$$\tilde{f}_{\rm det}(\mathbf{v}) = \tilde{f}_{\rm gal}(\mathbf{v} + \mathbf{v}_e(t)), \tag{4.2}$$

The equation $\mathbf{v}_e(t) = \mathbf{v}_{\rm LSR} + \mathbf{v}_\odot + \mathbf{v}_e^{\rm orb}(t)$ illustrates Earth's motion relative to the galactic frame, comprising three distinct elements. The component $\mathbf{v}_{\rm LSR} = (0, v_c, 0)$ signifies the motion of the Local Standard of Rest (LSR), with v_c representing the circular velocity at Sun's position. The component $\mathbf{v}_\odot = (U_\odot, V_\odot, W_\odot)$ is linked to the peculiar motion velocity vector of the Sun in relation to the LSR. Lastly, the component $\mathbf{v}_e^{\rm orb}(t)$ defines the Earth's orbital movement around the Sun, represented as $\mathbf{v}_e^{\rm orb}(t) = v_e^{\rm orb}\left[\hat{e_1}\sin\lambda(t) - \hat{e_2}\cos\lambda(t)\right]$ [29], where $v_e^{\rm orb} = 29.8\,{\rm km/s}$. Here, $\lambda(t)$ denotes the solar ecliptic longitude. The orthogonal unit vectors $\hat{e_1} = (-0.0670, 0.4927, 0.8676)$, and $\hat{e_2} = (-0.9931, -0.1170, 0.01032)$, defining Earth's plane during the spring equinox and summer solstice respectively, are expressed in galactic coordinates.

The Earth's periodic revolution around the Sun results in the annual modulation of the scattering event rate. This modulation stands out as one of the most conspicuous features in dark matter detection and acts as a significant tool to discern between signal and background [23]. We consider a constant $v_c = 220$ km/s and simplify our model by overlooking the Earth's orbit's minor eccentricity. Subsequently, we focus on the annual time-averaged halo integrals, representing an average over the course of one year.

Figure 4.1 illustrates the time-averaged halo integrals as a function of $v_{\rm min}$ in the vicinity of the Sun, focusing on the best fit Sun's position. This analysis is based on the closest snapshot to the LMC's pericenter approach and involves four distinct halos (halos 2, 6, 13, and 15), as shown in figure 3.3. The arrangement of the halos is as follows: halo 2 in the top left, halo 6 in the top right, halo 13 in the bottom left, and halo 15 in the bottom right panel.

The halo integrals are computed using the average velocity distributions of dark matter particles from both the Milky Way and the LMC, depicted by black solid lines, and from the Milky Way-only, represented by red solid lines. The uncertainty in these halo integrals, indicated by shaded bands, is derived

from the dark matter velocity distribution at one standard deviation from the mean.

Additionally, the lower panels of the figure present the relative differences between the halo integrals of the combined Milky Way+LMC system and those of the Milky Way-only. This difference is quantified as $(\eta_{\rm MW+LMC}-\eta_{\rm MW})/\eta_{\rm MW}$, offering insights into the impact of the LMC's presence on the dark matter distribution in the Solar neighborhood.

4.2 Variations across halos and snapshots

Figure 4.1 shows notable distinctions in the halo integrals between the Milky Way+LMC and the Milky Way-only scenarios. Specifically, halos 6 and 15 exhibit discrepancies in their halo integral tails, with halo 6 showing a relative difference of ~ 6, and halo 15 having a difference ~ 0.5. In contrast, halos 2 and 13 display minimal variation between the Milky Way+LMC and Milky Way-only cases. Their relative differences are notably less, being < 0.1 for halo 2 and ~ 0.01 for halo 13. Interestingly, despite halo 13 possessing a greater $\kappa_{\rm LMC}$ in the Solar region than the other three halos, it does not exhibit significant deviations. This underscores the critical role of the LMC's speed distribution's specific shape and peak speed in the detector's reference frame within the Solar neighborhood of each Milky Way analogue.

In order to assess variations in the tails of the halo integrals for both native dark matter particles belonging to the Milky Way and the cumulative dark matter particles originating from the Milky Way+LMC system, we introduce a dimensionless parameter, denoted as $\Delta\eta$, expressed as:

$$\Delta\eta = \sum_{v^i_{\rm min}\geq 0.7 v^{\rm det}_{\rm esc}} \left[\eta_{\rm MW+LMC}(v^i_{\rm min}) - \eta_{\rm MW}(v^i_{\rm min})\right] \Delta v_{\rm min} \ , \tag{4.3}$$

Here, $\Delta v_{\rm min}$ represents the bin size in $v_{\rm min}$, while $v^i_{\rm min}$ signifies the midpoint of these bins in $v_{\rm min}$, at which the halo integrals are computed for both Milky Way+LMC, denoted as $\eta_{\rm MW+LMC}$, and Milky Way-only, denoted as $\eta_{\rm MW}$. The summation encompasses all bins for which $v^i_{\rm min}$ exceeds 70% of the local escape

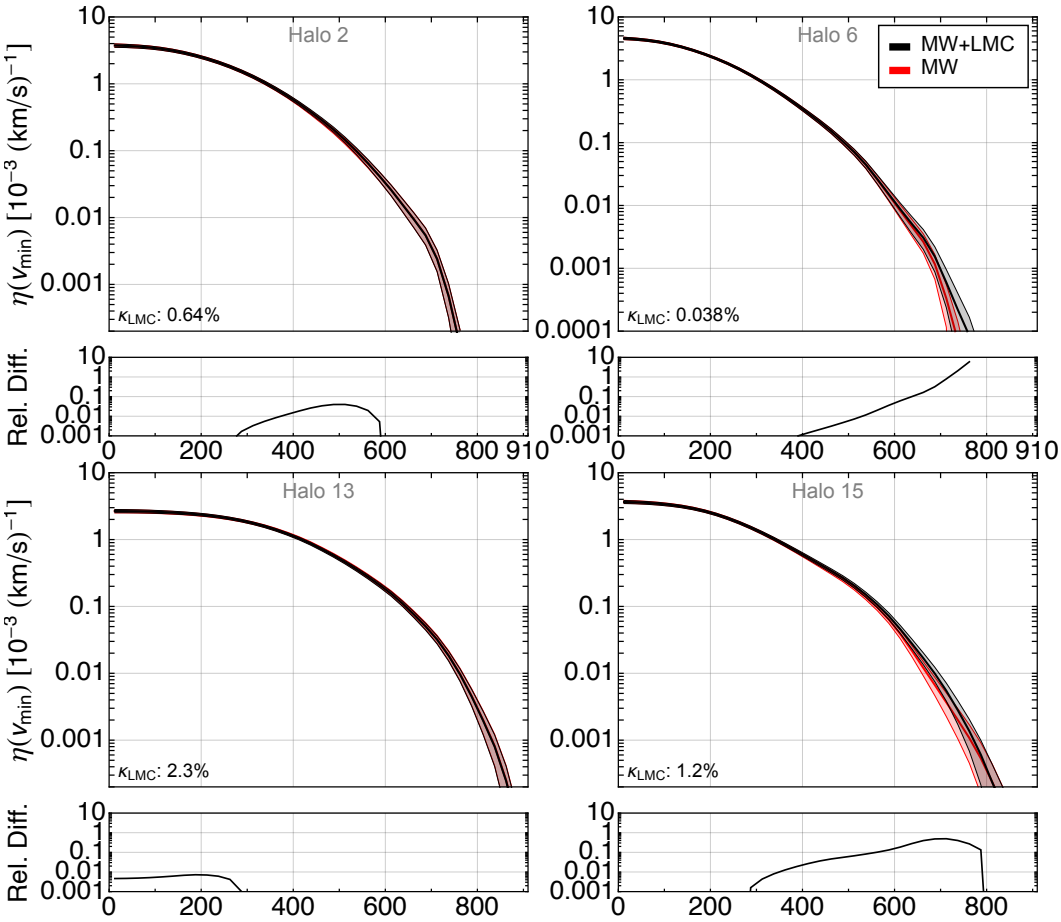

Figure 4.1: The time-averaged halo integrals in the vicinity of the Sun for four distinct halos: 2, 6, 13, and 15, specifically during the snapshot nearest to the LMC's closest approach to the pericenter. Presented in four panels, with halos 2, 6, 13, and 15 depicted in the top left, top right, bottom left, and bottom right, respectively, for the best fit Sun's position. The black curves illustrate the halo integrals comprising dark matter particles from both the Milky Way and the LMC (MW+LMC), and the red curves for those from the Milky Way-only. The solid lines in each graph represent the halo integrals derived from the average dark matter velocity distribution, while the shaded areas indicate the range of dark matter velocity distribution at 1σ deviation from the mean. Additionally, the specific value of $\kappa_{\rm LMC}$ is indicated in each panel. Below these plots, the relative discrepancies between the halo integrals of the combined Milky Way+LMC system and the Milky Way-only, expressed as $(\eta_{\rm MW+LMC} - \eta_{\rm MW})/\eta_{\rm MW}$, are shown. (figure from ref. [60])

speed from the Milky Way in the rest frame of the detector, indicated as $v_{\rm esc}^{\rm det}$. The value of $v_{\rm esc}^{\rm det}$ is estimated based on the largest $v_{\rm min}$ where $\eta_{\rm MW}$ has a non-zero value. Specific values for $v_{\rm esc}^{\rm det}$ within the Solar region, obtained for the best fit position of the Sun in 15 Milky Way-LMC analogues, are provided in

table 3.1. These values are derived from the simulation snapshot closest to the LMC's approach to its pericenter.

It is worth noting that $v_{\min}$ exhibits an inverse relationship with the dark matter mass, as indicated by eqs. (5.2) and (5.6). This inverse dependence on dark matter mass renders the exclusion limits of direct detection experiments highly responsive to even minor fluctuations in the high speed tails of the halo integrals, particularly for low dark matter masses. To address this sensitivity, we introduced the parameter $\Delta\eta$, which specifically encompasses variations in the tail of the halo integral and direct detection exclusion limits for $v_{\min}$ values exceeding 70% of $v_{\text{esc}}^{\text{det}}$. This numerical approach offers a representation of the fluctuations in direct detection exclusion limits at the low dark matter mass range.

We have explored alternative metrics for $\Delta\eta$, such as the relative difference, the divergence in the curve's area, and various fractions of $v_{\text{esc}}^{\text{det}}$ within the aforementioned metric. All these alternatives reveal analogous overarching trends. Nevertheless, the present definition retains these global features while also establishing an intuitive link between the halo integral plots and the ensuing direct detection exclusion limits.

In our analysis, we have identified three pivotal factors contributing to variations in the tails of the halo integrals. These factors encompass:

1. The proportion of dark matter particles originating from the LMC within the Solar vicinity.

2. The positioning of the Sun (and consequently, the delineation of the "Solar neighborhood") within our simulations.

3. The Milky Way's response, which arises due to the LMC's movement during its orbit near pericenter.

In the subsequent sections, we will delve into a detailed discussion of how these phenomena individually impact our findings.

4.3 Impact of the dark matter particles originating from the LMC

Dark matter particles from the LMC, upon reaching infall, attain velocities sufficient to escape the LMC's gravitational pull. A portion of these particles reaches the vicinity of the Sun within the Milky Way. These LMC-originated dark matter particles are typically faster than the Milky Way's native dark matter particles, influencing the tails of the halo integrals. An increase in the $\kappa_{\rm LMC}$ parameter signifies a more noticeable impact on these integrals.

In figure 4.2, the relationship between $\kappa_{\rm LMC}$ (the proportion of dark matter particles from the LMC near the Solar region) and the alteration in the halo integral's tail, denoted as $\Delta\eta$ (as per eq. (4.3)), is depicted. This figure compares three scenarios: the best fit position of the Sun (represented by black squares), the Solar region maximizing $\Delta\eta$ (indicated by yellow dots), and the Solar region where $\Delta\eta$ is minimized (blue dots). The figure's left panel presents data from 15 Milky Way-LMC analogues at the time closest to the LMC's pericenter approach. The right panel, on the other hand, displays various stages of halo 13, from approximately 314 Myr before to around 175 Myr after the present time.

In both panels, it is observed that the $\Delta\eta$ for the Sun's best fit position is typically near or at the maximum $\Delta\eta$ value, both increasing alongside $\kappa_{\rm LMC}$ in the Solar region. The minimum $\Delta\eta$ is either zero or nearly zero for several Milky Way-LMC analogues and specific phases of halo 13, yet an upward trend with $\kappa_{\rm LMC}$ is still evident in halo 13. As elaborated earlier, $\kappa_{\rm LMC}$ tends to rise with the LMC to Milky Way mass ratio at infall ($M^{\rm LMC}_{\rm Infall}/M^{\rm MW}_{200}$). Thus, a larger mass ratio between the LMC and Milky Way generally leads to a more substantial $\Delta\eta$, although this is dependent on the specific position of the Sun.

Figure 4.3 shows the changes in $\Delta\eta$ within halo 13. It displays the variation of $\Delta\eta$ at the Solar region, corresponding to the best fit Sun's positions, across different snapshots. These snapshots are charted relative to the present day snapshot, denoted as $t - t_{\rm Pres.}$. A color bar in the figure indicates the $\kappa_{\rm LMC}$ range. Notably, the snapshots coinciding with the highest $\kappa_{\rm LMC}$ values,

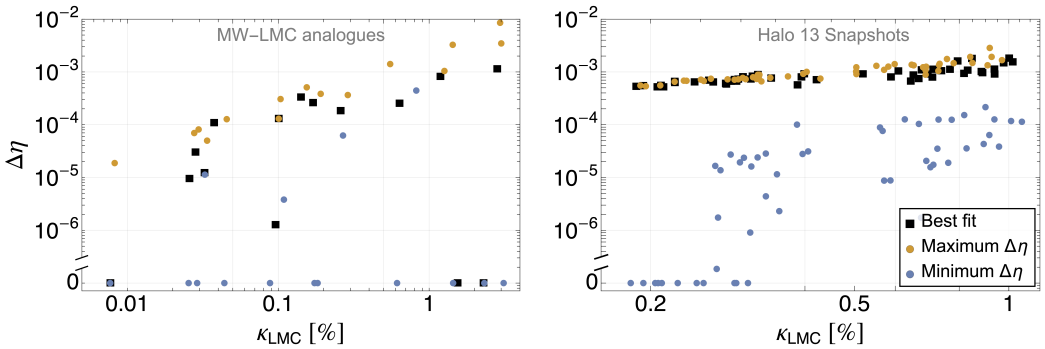

Figure 4.2: The relationship between $\Delta\eta$ (the variation in the halo integral's tail due to LMC particles) and $\kappa_{\rm LMC}$ is analyzed for three distinct Solar regions: the best fit Sun's position (indicated by black squares), the region where $\Delta\eta$ is maximized (yellow dots), and the region with the minimum $\Delta\eta$ (blue dots). The study is illustrated in two panels. The left panel focuses on 15 Milky Way-LMC analogues, specifically at the time frame closest to the LMC's pericenter approach. In contrast, the right panel examines various snapshots of halo 13, spanning from approximately 314 Myr before to roughly 175 Myr after the present day snapshot. This analysis provides insights into how $\Delta\eta$ and $\kappa_{\rm LMC}$ are correlated under different conditions and time frames. (figure from ref. [60])

especially around the LMC's pericenter approach, also exhibit the greatest $\Delta\eta$ values. Conversely, snapshots more distant from the pericenter show reductions in both $\kappa_{\rm LMC}$ and $\Delta\eta$. The two snapshots at approximately 174 and 191 Myr before the present day are both highest in $\kappa_{\rm LMC}$, each at 1.0%. Among these, the one nearest to the pericenter snapshot (about 41 Myr before the LMC's pericenter approach) records the largest $\Delta\eta$.

Despite the clear correlation between $\Delta\eta$ and $\kappa_{\rm LMC}$, the variability in $\Delta\eta$ values persists among systems with equivalent or near-equivalent $\kappa_{\rm LMC}$ values. This variation is attributable to the specific selection of the Sun's position when defining the Solar region. This phenomenon is observable in both panels of figure 4.2, where significant discrepancies exist between the minimum and maximum $\Delta\eta$ for the same or similar $\kappa_{\rm LMC}$ values.

Consequently, our analysis extends beyond just the influence of $\kappa_{\rm LMC}$ on $\Delta\eta$. It also encompasses the effects of the precise Sun-LMC geometry and investigates whether the best fit Sun's position uniquely maximizes $\Delta\eta$. These aspects are further explored in the subsequent section.

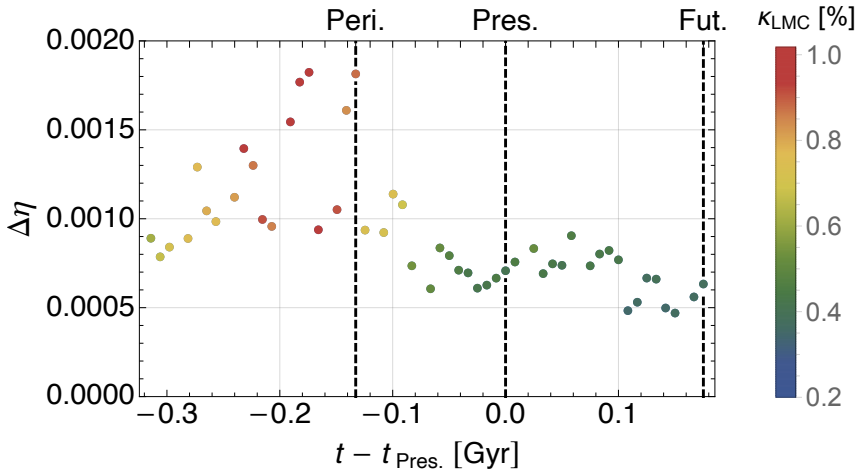

Figure 4.3: The plot of $\Delta\eta$ within the Solar region, corresponding to the best fit Sun's positions in halo 13, is set against the timeline of snapshots relative to the present day, denoted as $t - t_{\rm pres}$. This timeline extends from approximately 314 Myr prior to the present day to about 175 Myr subsequent to it. A color bar within the plot indicates the range of $\kappa_{\rm LMC}$. Noteworthy points in time, including the LMC's pericenter approach (Peri.), the present day (Pres.), and a future point around 175 Myr after the present day (Fut.), are highlighted with vertical dashed black lines in the plot. (figure from ref. [60])

4.4 Variation due to the Sun-LMC geometry

In the examination of 15 Milky Way-LMC analogues, a significant degree of variation in $\kappa_{\rm LMC}$ values is observed, primarily influenced by the selection of the Solar region. Specifically, $\kappa_{\rm LMC}$ can fluctuate by about a factor of 2, contingent on the particular Milky Way-LMC analogue (as exemplified in the last column of table 3.1). Furthermore, even when Solar regions share comparable $\kappa_{\rm LMC}$ values, there is a notable dispersion in the extent to which the tails of the combined Milky Way+LMC halo integrals diverge from those of the Milky Way-only.

This phenomenon is also visible in figure 4.1. Here, the most substantial deviation in the halo integral's tail is observed in halo 6, where $\kappa_{\rm LMC}$ is 0.038%, contrasting with halo 13 that, despite having the highest $\kappa_{\rm LMC}$ of 2.3%, exhibits only minimal variation.

These observations underscore that while $\kappa_{\rm LMC}$ is a crucial factor in determining $\Delta\eta$, the specific Sun-LMC spatial arrangement within the chosen Solar

region holds comparable significance.

Figure 4.4 presents time-averaged halo integrals for both the Milky Way+ LMC (in black) and Milky Way-only (in red) dark matter populations. These are specifically for the current snapshot of halo 13, covering two distinct Solar regions: the best fit Sun's position (left panel) and the Solar region minimizing $\Delta\eta$ (right panel). Each panel also details the $\kappa_{\rm LMC}$ value and the cosine angles correlating with the Sun's position, as defined in eq. (2.1). Beneath the halo integral plots, sub-panels illustrate the relative differences between the Milky Way+LMC and Milky Way-only integrals. A noticeable divergence is seen in the tail of the Milky Way+LMC halo integral at the best fit Sun's position, in contrast to minimal variations in the region minimizing $\Delta\eta$. This underscores the significance of the Sun-LMC spatial relationship, demonstrating how identical snapshots with comparable $\kappa_{\rm LMC}$ values can exhibit significant differences in the halo integral tails based on the chosen Sun's position.

To disentangle the influence of the Sun-LMC geometry from that of $\kappa_{\rm LMC}$ on $\Delta\eta$, the study examines cosine angles that characterize the Sun-LMC geometry, as per eq. (2.1). Figure 4.5 maps the permissible Sun positions in the parameter space defined by these two cosine angles for halo 13 at the present day snapshot. The color bars in each panel indicate the range of $\kappa_{\rm LMC}$ and $\Delta\eta$, respectively. The observed values of the cosine angles, derived from eq. (2.2), are marked with a black square in each panel. A comparison of the two panels reveals that the maximum $\Delta\eta$ is located in the quadrant where both $\cos\alpha$ and $\cos\beta$ are negative, contrasting with the quadrant where $\kappa_{\rm LMC}$ peaks, characterized by positive $\cos\alpha$ and $\cos\beta$.

On average, the $\kappa_{\rm LMC}$ value experiences an average variation of 0.15% among the different permissible Sun positions within a specific snapshot. However, this variation can escalate to as much as one percent when comparing across different snapshots. Consequently, within a single snapshot, the primary determinant of $\Delta\eta$ is the specific geometry of the Sun-LMC configuration. Moreover, an analysis across various snapshots reveals that the highest values of $\Delta\eta$ are predominantly found in quadrants where $\cos\beta$ is negative. This negative $\cos\beta$ implies an oppositional direction between the velocity vec-

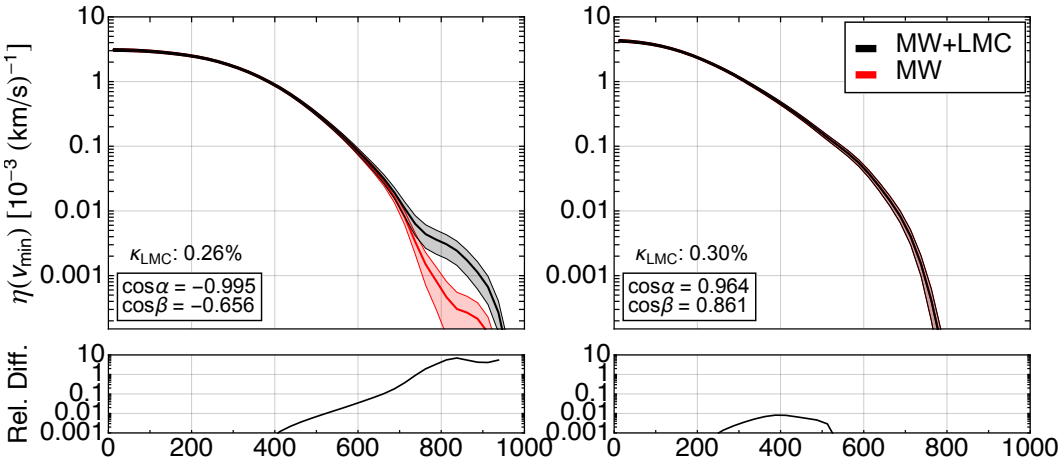

Figure 4.4: For the present day snapshot of the halo 13, the time-averaged halo integrals for both the Milky Way+LMC (illustrated in black) and Milky Way-only (depicted in red) dark matter populations are presented. This comparison is shown for two distinct scenarios: the best fit position of the Sun (left panel) and the Solar region exhibiting the lowest $\Delta\eta$ (right panel). The halo integrals derived from the average dark matter velocity distribution are represented by solid lines, whereas those computed from the dark matter velocity distribution at 1σ from the mean are indicated by shaded bands. Additionally, the value of $\kappa_{\rm LMC}$ and the cosine angles (as defined in eq. (2.1)) are detailed in each panel. Subsequently, the lower panels depict the relative differences between the halo integrals for the combined Milky Way+LMC and the Milky Way-only scenarios. (figure from ref. [60])

tors of the LMC analogue and the Sun, resulting in higher relative speeds for the LMC-originating particles relative to the Sun, thereby amplifying $\Delta\eta$. Given that the observed cosine angles are also negative, it suggests that the variations in the halo integral's tail at the best fit Sun's position are proximate to the maximum possible variation relative to other permissible Sun positions. This observation aligns with the data presented in figure 4.2, where the $\Delta\eta$ values for the best fit Sun's positions (black squares) approximate the highest $\Delta\eta$ values (yellow dots).

Consequently, it can be inferred that the best fit Sun's position does indeed occupy a privileged stance in maximizing $\Delta\eta$. This is attributed to the observed negative $\cos\beta$, indicating a general opposition in the directions of the Sun's and the LMC's velocities. Such a scenario suggests that for the actual Milky Way, the influence of the LMC is likely to be maximally impactful on

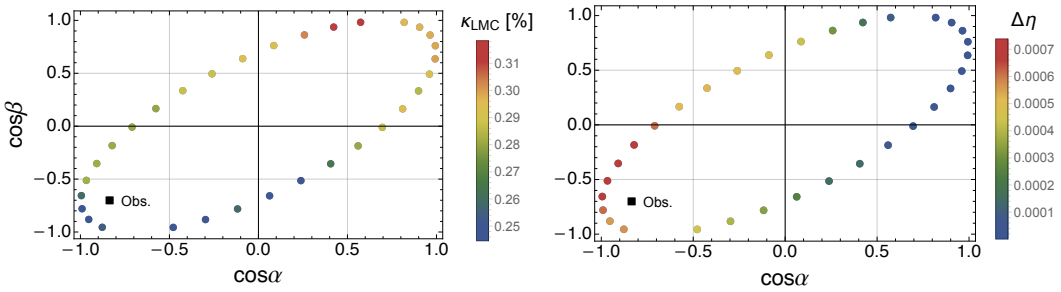

Figure 4.5: The present day snapshot of halo 13 showcases the cosine angles, which are crucial in defining the Sun-LMC geometry (eq. (2.1)). This is depicted for all permissible positions of the Sun, with each position color-coded based on the value of $\kappa_{\rm LMC}$ (left panel) and $\Delta\eta$ (right panel). Moreover, the observed values of these cosine angles (detailed in eq. (2.2)) are distinctly marked with a black square on each panel. (figure from ref. [60])

the tail of the halo integral.

Our investigation also encompassed how the magnitude of $\Delta\eta$ for the present day snapshot of halo 13 is influenced by the dimensions of the defined Solar region. We observed that a reduction in the Solar region's size notably enhances $\Delta\eta$, attributable to heightened sensitivity towards the best fit Sun's position. Specifically, when the cone's opening angle is narrowed from $\pi/4$ to $\pi/6$, while maintaining the same spherical shell width, there is an 18% increase in $\Delta\eta$. Conversely, lessening the shell width to $7-9$ kpc, while retaining the original cone opening angle, results in a more modest 7% rise in $\Delta\eta$. A more substantial increase of 78% in $\Delta\eta$ is realized when both the cone's opening angle is reduced to $\pi/6$ and the shell width is narrowed to $7-9$ kpc. However, this adjustment drastically lowers the count of dark matter particles from both the Milky Way and LMC within the Solar region, thereby introducing significant Poisson uncertainties. Hence, our findings are conservative regarding the Solar region's size.

On the other hand, expanding the Solar region size slightly diminishes $\Delta\eta$, stemming from a reduced sensitivity to the best fit Sun's position. To illustrate, widening the cone's opening angle from $\pi/4$ to $\pi/2$, while the spherical shell width remains unchanged, leads to a mere 2% decrease in $\Delta\eta$.

4.5 Milky Way's response to the LMC

The influence of the LMC on the Solar region, particularly on the high-velocity end of the local dark matter velocity distribution, is a key factor in understanding the local dark matter halo dynamics of the Milky Way. This influence is not only due to particles directly emanating from the LMC, but also arises from the Milky Way's dynamical reaction to the LMC's orbital path. Prior studies have observed and analyzed the Milky Way's reaction to the LMC in simplified models [12][22]. However, examining this reaction in a fully cosmological context, which accounts for the complex accretion history of halos, is crucial. This section delves into how the Milky Way's response impacts the high speed tail of the halo integral in our cosmological simulations and differentiates this effect from the high speed dark matter particles in the Solar region originating from the LMC.

In figure 4.6, we analyze the time-averaged halo integrals for four distinct snapshots of halo 13. These snapshots include: the isolated Milky Way analogue (Iso.), the LMC's closest approach (Peri.), the current Milky Way-LMC state (Pres.), and a projected future Milky Way-LMC state (Fut.). For the last three states, we present the halo integrals for both the combined Milky Way+LMC system (solid curves) and the Milky Way alone (dashed curves), based on the optimal position of the Sun. The isolated Milky Way state, which lacks an LMC-like satellite, has its halo integral (solid black curve) derived from dark matter particles in a spherical shell around the Galactic center, with radii ranging from 6 to 10 kpc. For context, we include a comparison with the halo integral from a Maxwellian velocity distribution, which assumes a peak speed of 220 km/s and is truncated at the escape velocity of 544 km/s, a common approach in the SHM.

Analyzing the halo integrals of the Milky Way at different stages, both isolated and influenced by the LMC, reveals the dynamic response of the Milky Way's native dark matter in the Solar region. Initially, the halo integral of the isolated Milky Way, represented approximately 2.8 Gyr before the current era, acts as a baseline (solid black curve). This snapshot, depicting the Milky

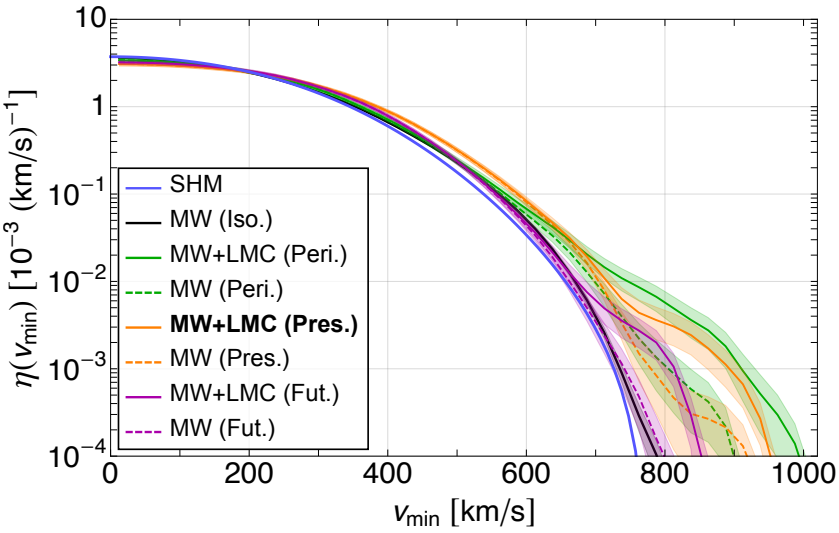

Figure 4.6: The figure presents time-averaged halo integrals from four specific stages in halo 13, encompassing different phases of the Milky Way and LMC interaction. These phases include: the isolated Milky Way snapshot (Iso.), the LMC at its closest approach to the Milky Way (Peri.), the present day Milky Way-LMC configuration (Pres.), and a projected future Milky Way-LMC snapshot (Fut.). In these snapshots, solid and dashed lines, along with shaded areas, represent halo integrals derived from the average dark matter velocity distribution and the dark matter velocity distribution within one standard deviation (1σ) from the mean, respectively. For the scenarios involving the present, pericenter, and future states, we display halo integrals for the best fit Solar region in two contexts: the combined Milky Way+LMC dark matter populations (solid curves) and the Milky Way-only dark matter populations (dashed curves). In contrast, the isolated Milky Way phase, devoid of an LMC counterpart, features its Milky Way halo integral (solid black curve) calculated for a Solar region defined as a spherical shell with radii ranging from 6 to 10 kpc from the Galactic center. Furthermore, the study includes a solid blue curve illustrating the SHM halo integral, which is derived from a Maxwellian velocity distribution. This distribution is characterized by a peak speed of 220 km/s and is truncated at the Galaxy's escape speed of 544 km/s. (figure from ref. [60])

Way without LMC's impact, aligns closely with the SHM, although it exhibits a slightly more extended tail, reaching a minimum velocity ($v_{\rm min}$) of about 800 km/s.

A significant variation occurs when the LMC approaches its first pericenter. At this time, the Milky Way's native dark matter halo integral (dashed green curve) demonstrates an enhanced tail, extending to $v_{\rm min} \approx 900$ km/s. This

enhancement is also observed in the present day snapshot (dashed orange curve), where the LMC is close to its pericenter, indicating a similar boost in the tail of the halo integral.

In a future scenario, approximately 175 Myr after the present day, the halo integral for the Milky Way's local dark matter (dashed magenta curve) reverts to a tail similar to the isolated Milky Way state, with $v_{\min}$ returning to $\sim$ 800 km/s. This future state mirrors the effects observed in the Auriga simulations, where a satellite galaxy's passage through a host dark matter halo creates a comparable overdensity wake. This period is akin to the overdensity wake induced in a host dark matter halo by a satellite galaxy's passage in the Auriga simulations [34].

During the pericenter snapshot, characterized by the highest LMC contribution ($\kappa_{\mathrm{LMC}} = 0.85\%$), the combined Milky Way+LMC halo integral (solid green curve) exhibits the most pronounced increase in tail speed, reaching approximately 1000 km/s. This represents an increase of about 100 km/s over the tail speed of the Milky Way-only integral. Similarly, the present day snapshot, with a κ_{LMC} value of 0.26%, shows a substantial disparity between the Milky Way+LMC and Milky Way-only halo integrals at higher velocities. In a future Milky Way-LMC scenario ($\kappa_{\mathrm{LMC}} = 0.22\%$), the Milky Way+LMC halo integral's tail is elevated by $\sim$ 50 km/s compared to the Milky Way-only integral.

When contrasting these observations with the boost in the native Milky Way dark matter population at pericenter and present day snapshots, it is apparent that the influence of LMC-origin dark matter particles on the halo integral's tail is comparable in magnitude. Figure 4.6 illustrates this effect: the dark matter particles in the Solar neighborhood, which normally reach speeds around 800 km/s in the absence of LMC influence (solid black curve), are accelerated to over 950 km/s in the current era (solid orange curve). This escalation, exceeding 150 km/s, results from both the Milky Way's response and the incorporation of high speed LMC particles in the Solar region.

Chapter 5

Implications for dark matter direct detection

This chapter elaborates on how the LMC influences the interpretation of dark matter direct detection experiments. Specifically, we analyze dark matter interactions with either a nucleus or an electron in sections 5.1 and 5.2. We examine the modifications in the exclusion limits for dark matter mass and scattering cross section in various direct detection experiments due to the LMC's presence, considering specific experimental setups.

Our study simulates signals for three hypothetical direct detection experiments, modeled after upcoming detectors aiming to detect nuclear or electron recoils caused by dark matter particle interactions. To determine the constraints on the dark matter scattering cross section and mass, we use the Poisson likelihood method as implemented in the DDCalc [17] and QEDark [31][25] software for nuclear and electron recoils, respectively. These tools, utilizing the properties of the experimental setups and the local dark matter distribution, calculate exclusion limits at a specified confidence level. For our direct detection analysis, we directly incorporate local dark matter velocity distributions obtained from simulations.

5.1 Dark matter - nucleus scattering

In the context of dark matter interactions with atomic nuclei, we analyze a scenario where a dark matter particle of mass m_χ collides with a nucleus

(mass m_T) within an underground detector, imparting a specific amount of recoil energy E_R. The rate of such events is differential and can be expressed as:

$$\frac{dR}{dE_R} = \frac{\rho_\chi}{m_\chi}\frac{1}{m_T}\int_{v>v_{\min}} d^3v \; \frac{d\sigma_T}{dE_R} \; v \; \tilde{f}_{\rm det}(\mathbf{v}, t) \; , \tag{5.1}$$

In this expression, σ_T represents the cross section of dark matter-nucleus scattering.

When considering elastic scattering phenomena, the lowest velocity $v_{\min}$ necessary for a dark matter particle to transfer recoil energy E_R to the detector can be described by the equation:

$$v_{\min}(E_R) = \sqrt{\frac{m_T E_R}{2\mu_{\chi T}^2}} \; , \tag{5.2}$$

Here, $\mu_{\chi T}$ denotes the reduced mass of the dark matter particle and the target nucleus.

In the analysis of spin-independent interactions, the differential cross section can be articulated as follows:

$$\frac{d\sigma_T}{dE_R} = \frac{m_T A^2 \sigma_{\chi N}^{\rm SI}}{2\mu_{\chi N}^2 v^2} \, F^2(E_R) \; , \tag{5.3}$$

In this equation, A represents the atomic mass number of the target nucleus, $\sigma_{\chi N}^{\rm SI}$ is the spin-independent dark matter-nucleon scattering cross section at zero momentum transfer, $\mu_{\chi N}$ denotes the reduced mass between the dark matter particle and nucleon, and $F(E_R)$ is the nuclear form factor for spin-independent interaction, with the Helm form factor as the reference model [37].

Consequently, the differential event rate, in terms of the halo integral (eq. (4.1)), is expressed as:

$$\frac{dR}{dE_R} = \frac{\rho_\chi A^2 \sigma_{\chi N}^{\rm SI}}{2 m_\chi \mu_{\chi N}^2} \, F^2(E_R) \, \eta(v_{\min}, t) \, . \tag{5.4}$$

In this study, we examine two idealized direct detection experiments targeting dark matter: one employing a xenon-based detector, and the other utilizing germanium. These conceptual models draw upon the anticipated sensitivity of upcoming LZ [1][5] and SuperCDMS [4] experiments. Noble liquid detectors like LZ, which have recently reported initial findings [1], offer the capability

of extensive exposure, adept at detecting larger dark matter masses and reduced cross sections. Conversely, cryogenic solid-state detectors, exemplified by SuperCDMS, excel in detecting dark matter masses below 1 GeV. Collectively, these detector types cover a broad spectrum of dark matter masses and scattering cross sections.

The xenon-based detector under consideration is designed to operate within an energy window of $[2-50]$ keV. It features an energy resolution described by $\sigma_E = 0.065E_R + 0.24\,\mathrm{keV}\sqrt{E_R/\mathrm{keV}}$ [11] and is projected to achieve an exposure of 5.6×10^6 kg days, with a peak efficiency of 50% as outlined in ref. [5]. This level of exposure is anticipated for the LZ experiment over a five-year operational period [5].

Regarding the germanium-based detector, we assess two distinct crystal target configurations, each with a different energy threshold. The first, a low energy threshold model, is inspired by the proposed high-voltage (HV) detector of the SuperCDMS SNOLAB project [4]. It is set to monitor an energy interval of $[40-300]$ eV, maintaining a steady signal efficiency of 85%, a uniform background of 10 keV^{-1} kg^{-1} days^{-1}, and an exposure of 1.6×10^4 kg days [4][41]. The second design, with a higher energy threshold, shares characteristics with the iZIP detector of the same experiment. This design includes an exposure of 2.04×10^4 kg days, an energy range of $[3-30]$ keV, an anticipated single background event, and a consistent efficiency of 75%. The exposures for both designs are projected to be attainable by SuperCDMS after a five-year exposure [4].

In the upper panels of figures 5.1 and 5.2, the 90% confidence level (CL) exclusion limits are displayed in the plane of dark matter mass and spin-independent cross section. These limits are derived from anticipated xenon and germanium experiments, which utilize the local dark matter velocity distribution captured in four distinct snapshots of halo 13. The snapshots include the isolated Milky Way analogue (Iso.), the LMC's pericenter approach (Peri.), the present day Milky Way+LMC analogue (Pres.), and the projected future Milky Way+LMC scenario (Fut.).

The exclusion limits, represented by both a mean line and a shaded area,

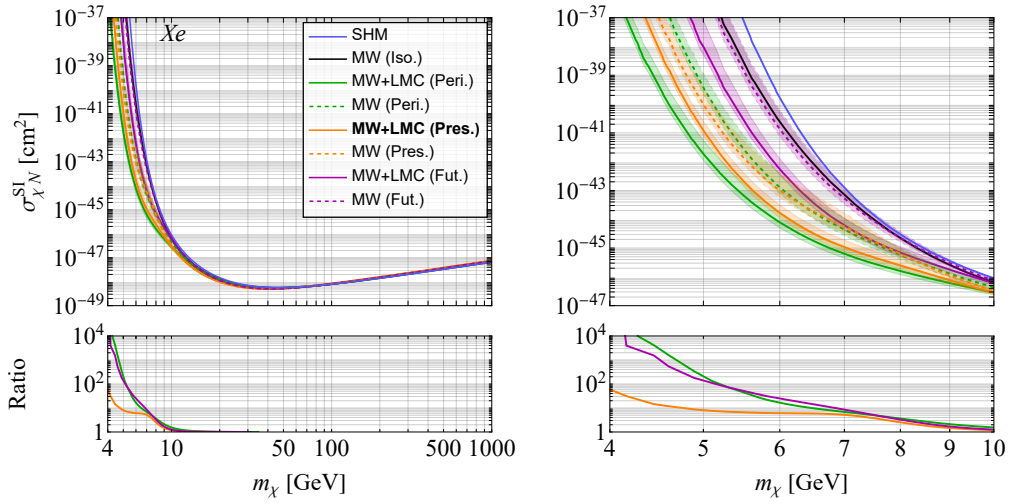

Figure 5.1: The upper panels illustrate the 90% confidence level (CL) exclusion limits for a prospective xenon-based experiment, mapping the spin-independent dark matter-nucleon cross section against dark matter mass. These limits are showcased for four distinct snapshots in halo 13: the isolated Milky Way analogue (Iso.), the LMC's pericenter approach (Peri.), the present day Milky Way-LMC analogue (Pres.), and a future projection of the Milky Way-LMC analogue (Fut.). In each scenario, solid and dashed lines, along with shaded areas, represent the exclusion limits derived from the mean and the 1σ uncertainty range of the halo integrals, respectively. For the pericenter, present, and future snapshots, the exclusion limits are depicted in the Solar region, highlighting the most probable position of the Sun in both the combined Milky Way+LMC (solid colored curves) and the Milky Way-only (dashed colored curves) dark matter distributions. For the isolated Milky Way snapshot, the limit is indicated for the Milky Way's dark matter population (solid black curve) within a Solar region defined as a spherical shell spanning radii of 6 to 10 kpc from the Galactic center. The blue curve represents the exclusion limit for the SHM Maxwellian. A local dark matter density of $\rho_\chi = 0.3$ GeV/cm^3 is assumed. In the lower panels, the ratios of the exclusion limits between the Milky Way-only and Milky Way+LMC dark matter distributions for the pericenter, present, and future snapshots are presented. The left panels provide a broad overview of these limits and ratios across a wide dark matter mass spectrum, while the right panels focus specifically on the lower dark matter mass range. (figure from ref. [60])

correspond to the average and the 1σ uncertainty range of the halo integrals indicated in figure 4.6. The solid black curve denotes the exclusion limit for the isolated Milky Way analogue. In contrast, the exclusion limits for the remaining three snapshots feature solid colored lines for the combined

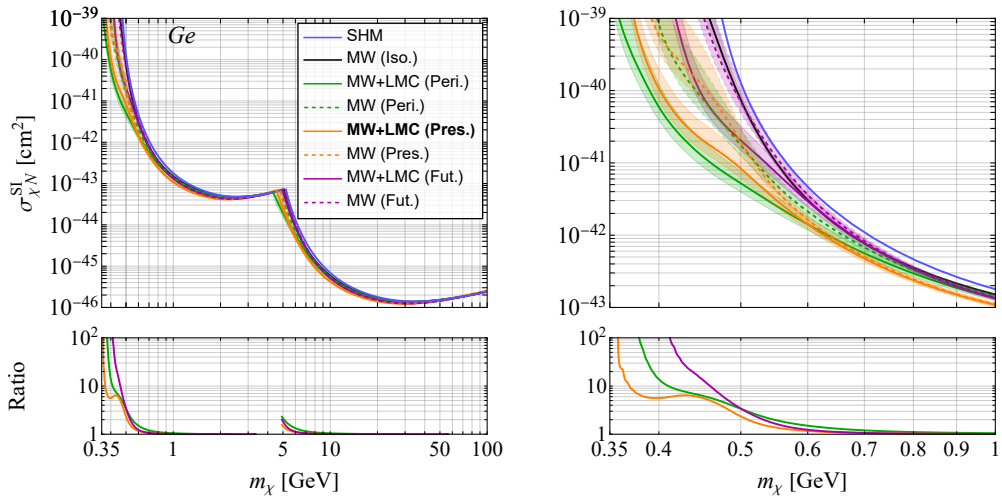

Figure 5.2: Similar to the representation in figure 5.1, this illustration pertains to a prospective germanium based experiment. (figure from ref. [60])

Milky Way+LMC distribution and dashed colored lines for the Milky Way-only scenario. Additionally, for comparative purposes, the exclusion limit based on the SHM Maxwellian velocity distribution, with a peak speed of 220 km/s and a cutoff at the galactic escape velocity of 544 km/s, is depicted as a solid blue curve. It is important to note that in all scenarios, the local dark matter density is consistently set to $\rho_\chi = 0.3$ GeV/cm^3, a standard assumption in the SHM. This density acts as a rate normalization factor, implying that any changes in its value would uniformly shift all exclusion limits up or down.

The lower panels of these figures highlight the ratio of the exclusion limits, comparing the Milky Way-only distribution with the combined Milky Way+LMC distribution for the pericenter, present day, and future snapshots. The left panels of these figures provide a broad overview of dark matter masses, while the right panels focus specifically on the lower dark matter mass range to enhance the visibility of differences in this range.

Analyzing the data in figures 5.1, 5.2, and 4.6, we observe comparable trends, particularly in the halo integrals of different snapshots. Notably, the variations in the high speed tails of these integrals significantly influence the exclusion limits at lower dark matter masses. This impact is most pronounced in areas where experiments exhibit heightened sensitivity to elevated $v_{\min}$ val-

ues. The exclusion limit is notably weaker for the isolated Milky Way snapshot at these lower dark matter masses, aligning closely with the SHM. Conversely, the dark matter distribution in the combined Milky Way+LMC, particularly at the LMC's pericenter approach, demonstrates the strongest exclusion limit.

Focusing on the xenon-based experiment detailed in figure 5.1, the present day Milky Way+LMC distribution's exclusion limit surpasses that of the isolated Milky Way. This difference is significant, reaching an order of magnitude at $m_\chi \sim 8$ GeV, over three orders at $m_\chi \sim 6$ GeV, and over five orders at $m_\chi \sim 5$ GeV. Additionally, for fixed cross sections, the Milky Way+LMC distribution at the present day snapshot exhibits a shift of several GeV towards smaller dark matter masses compared to the isolated Milky Way, for masses under $\mathcal{O}(10$ GeV).

In the context of the germanium-based experiment, as shown in figure 5.2, the exclusion limit difference between the present day Milky Way+LMC distribution and the isolated Milky Way reaches an order of magnitude at $m_\chi \sim 0.5$ GeV, and over three orders at $m_\chi \sim 0.4$ GeV. At fixed cross sections and for dark matter masses under $\mathcal{O}(1$ GeV), there is a notable horizontal shift of a few hundred MeV towards smaller dark matter masses. Thus, as figures 5.1 and 5.2 indicate, the LMC's inclusion extends the scope of direct detection experiments to smaller dark matter masses.

Our findings are in alignment with those presented in ref. [12]. The latter also indicates that the LMC's presence results in shifts to lower cross sections and dark matter masses in direct detection limits, thereby broadening the sensitivity range of these experiments. This confirms that the results of ref. [12] remain valid in a fully cosmological framework.

5.2 Dark matter - electron scattering

In the context of dark matter interacting with electrons, the differential event rate for a crystalline target is expressed as follows:

$$\frac{dR}{d\ln E_e} = N_{\text{cell}} \frac{\rho_\chi}{m_\chi} \frac{\overline{\sigma}_e \alpha m_e^2}{\mu_{\chi e}^2} \int d\ln q \, \frac{E_e}{q} \left[|F_{\text{DM}}(q)|^2 \, |f^{\text{crystal}}(E_e, q)|^2 \, \eta(v_{\min}(q, E_e)) \right] \,, \tag{5.5}$$

where the parameters are defined as follows: E_e denotes the energy transferred to the electron, q represents the momentum transfer in the dark matter-electron interaction, and $N_{\rm cell}$ indicates the number of unit cells in each mass unit of the crystal. The dark matter-electron reference cross section, $\overline{\sigma}_e$, characterizes the interaction strength, while $\alpha \simeq 1/137$ is the fine structure constant, m_e the electron mass, and $\mu_{\chi e}$ the reduced mass of the dark matter-electron. The factor $f^{\rm crystal}$, a dimensionless term, reflects the influence of the target material's electronic structure on the rate.

The form factor for dark matter, $F_{\rm DM}$, is crucial in understanding the momentum-based characteristics of the interaction. It is noted that for a heavy mediator in a contact interaction, $F_{\rm DM}(q)$ equals 1. For an electron dipole moment coupling, it becomes $(\alpha m_e/q)$, and for a long-range interaction mediated by an ultralight or massless mediator, it is expressed as $(\alpha m_e/q)^2$.

Furthermore, the minimum velocity ($v_{\rm min}$) that a dark matter particle must possess to impart an energy E_e to an electron, corresponding to the momentum transfer q, is given by:

$$v_{\rm min}(E_e, q) = \frac{E_e}{q} + \frac{q}{2m_\chi}\,. \tag{5.6}$$

In this study, we examine the potential of an upcoming silicon CCD experiment, leveraging the enhanced sensitivity anticipated in the kilogram-scale DAMIC-M project (referenced in [43], [20], [8]). Such experiments, which focus on the interactions between dark matter and electrons, are pivotal for investigating dark matter masses in the MeV range. This is primarily due to the electron's relatively small mass. Semiconductors are especially useful in this context because of their low ionization threshold, approximately 1 eV, enabling them to detect individual electron-hole pairs. We propose using a silicon detector with a total exposure of 1 kg year and assume zero background events, paired with a detection threshold of one electron-hole pair.

Figure 5.3 contains top panels that depict the 95% CL exclusion limits in the dark matter mass and dark matter-electron cross section plane. This is for the proposed silicon based experiment, considering various dark matter velocity distributions: the isolated Milky Way (black), pericenter (green), present

day (orange), and future projection (magenta) of halo 13. The exclusion limits for the latter three scenarios are represented as solid colored curves when considering both the Milky Way and LMC distributions, and as dashed curves for the Milky Way-only distribution. These limits, including their mean and the associated 1σ uncertainty band, are derived from the halo integrals shown in figure 4.6. The SHM exclusion limit is depicted as a solid blue curve. Regarding dark matter-nucleus scattering, the local dark matter density is assumed to be $\rho_\chi = 0.3$ GeV/cm^3. In the lower panels of the figure, the ratio of the exclusion limits for the Milky Way-only distribution to those of the combined Milky Way and LMC distributions are presented for the pericenter, present day, and future snapshots. Additionally, the left, middle, and right panels of the figure illustrate the results for three distinct dark matter form factors: $F_{\rm DM} = 1$, $F_{\rm DM} \propto q^{-1}$, and $F_{\rm DM} \propto q^{-2}$, respectively.

The influence of the LMC on the exclusion limits of the dark matter-electron scattering cross section bears similarities to its impact on dark matter-nucleus scattering, though to a lesser extent. As depicted in figure 5.3, the exclusion limits of the Milky Way combined with the LMC, both at the LMC's pericenter approach and in the present day Milky Way-LMC snapshots, exhibit a tendency towards lower dark matter masses and reduced dark matter-electron cross sections in comparison to the Milky Way in isolation. This shift is more pronounced at lower dark matter masses, where the experiments are sensitive to higher $v_{\rm min}$ values. Specifically, the present day Milky Way+LMC distribution's exclusion limit is approximately 4 times lower than that of the Milky Way alone for a dark matter mass of about 1 MeV, and roughly 50 times lower at 0.6 MeV. Below a few MeV in dark matter mass, the exclusion limit shifts downward by a fraction of an MeV for all three dark matter form factor options, given constant cross sections.

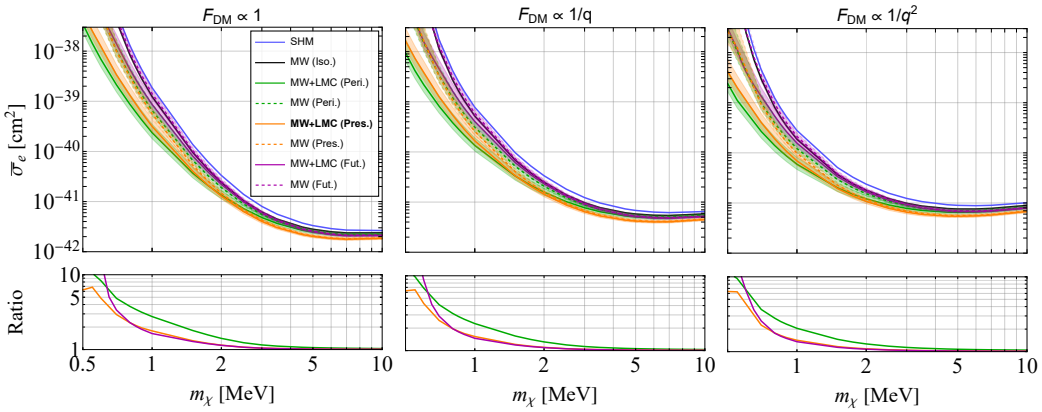

Figure 5.3: Upper panels: The 95% confidence level exclusion limits for an upcoming silicon based dark matter detection experiment are depicted, focusing on the dark matter-electron cross section and dark matter mass plane. These limits are analyzed for four distinct snapshots in halo 13: an isolated Milky Way analogue (Iso.), the LMC's pericenter approach (Peri.), the present day (Pres.), and a projected future snapshot (Fut.). Three dark matter form factors are examined: $F_{\rm DM} = 1$ (left), $F_{\rm DM} \propto q^{-1}$ (center), and $F_{\rm DM} \propto q^{-2}$ (right). The exclusion limit of the SHM is represented by the blue curve. The local dark matter density is consistently set at $\rho_\chi = 0.3$ GeV/cm^3. Lower panels: Presents the exclusion limit ratios comparing the Milky Way-only scenario to the combined Milky Way+LMC dark matter populations for the pericenter, present day, and future snapshots. The color-coded curve descriptions correspond to those outlined in figure 5.1. (figure from ref. [60])

Chapter 6

Discussion and conclusions

In this research, we employed magneto-hydrodynamical simulations from the Auriga project [35] to examine the influence of the LMC on the distribution of local dark matter and its subsequent effect on direct dark matter detection efforts. Our initial step was to select 15 Milky Way-LMC system analogues, based on the criteria that the LMC analogue's stellar mass and its distance to the host during its first pericenter approach concur with empirical observations.

Subsequently, our focus was narrowed to a singular Milky Way-LMC analogue. We analyzed how the LMC's presence alters the local dark matter distribution at various stages of its orbit. We specifically examined four critical snapshots: the isolated Milky Way analogue, the first pericenter approach of the LMC analogue, the snapshot nearest to the present day Milky Way-LMC configuration, and a projected future snapshot of the Milky Way-LMC system, approximately 175 Myr from the present day.

In our analysis, we extracted data regarding the dark matter density and velocity within the Solar neighborhood. We meticulously selected positions for the Sun in our simulations to align with the observed Sun-LMC geometry. This process involved determining the orientations of the stellar disks in the simulations to have the same angle with the LMC analogues' orbital plane, as in real-world observations. For each orientation, we specified the Sun's position by matching the angles between the LMC's orbital angular momentum and the Sun's position and velocity vectors in the simulations with

their observed counterparts. The position that yielded the closest match with these angles was deemed the best fit Sun's position. Utilizing the local dark matter velocity distributions derived from our simulations, we computed halo integrals, emphasizing how the LMC alters their high speed tails.

To conclude our research, we simulated anticipated signals in three forthcoming direct detection experiments involving xenon, germanium, and silicon. These simulations considered dark matter-nucleus interactions in the first two materials and dark matter-electron interactions in silicon. We focused on assessing the impact of the LMC on the exclusion limits of these experiments. Our key findings are summarized below:

1. The data from selected Milky Way-LMC analogues indicate that the percentage of dark matter particles that have originated from the LMC and are now present in the Solar region lies in the range of $[0.0077 - 2.8]\%$. This range is due to the halo-to-halo variation in the results. Concurrently, an equally important aspect is the variation in local dark matter density, which is observed to be in the range of $[0.21 - 0.60]$ GeV/cm^3. This variability is dependent on the characteristics of each galactic halo, highlighting the complexity and diversity of galactic structures and their impact on the local dark matter distribution.

2. The local speed distribution of dark matter particles originating from the LMC is a subject of significant interest in understanding the dynamics of these particles within the Milky Way. Notably, this distribution peaks at the high speed tail of the dark matter particles of the Milky Way, specifically at speeds greater than 500 km/s with respect to the center of the Milky Way analogue. Moreover, this feature exhibits considerable halo-to-halo variation, underscoring the diverse nature of galactic environments. Additionally, a temporal analysis of these distributions, particularly through different snapshots within a single halo, reveals the impact of the LMC throughout its orbit around the Milky Way. This impact is observed not only at the time of the LMC's pericenter approach and the present day but also to about 175 Myr after the present day,

illustrating the long-term effects of the LMC on the local dark matter distribution.

3. The interaction of the LMC with the Milky Way manifests in a significant shift in the high speed tail of the halo integrals towards higher velocities. This shift can be understood through three primary contributing factors, as encapsulated by the metric $\Delta\eta$ (see eq. 4.3). The first factor is the relative abundance of dark matter particles from the LMC within the Solar region. A higher concentration of these particles generally corresponds to an increased value of $\Delta\eta$, a trend observed across different Milky Way-LMC analogues and at various points in time within a single system. The second factor concerns the geometrical positioning of the Sun relative to the LMC in the simulations. The impact of this Sun-LMC geometry on $\Delta\eta$ is significant, with the best-fit Sun's position being one that maximizes this metric. This suggests that $\Delta\eta$ should be close to its maximum value in the actual Milky Way. The third factor is the response of the native dark matter particles in the Milky Way to the LMC's passage. This response, characterized by an acceleration of the native dark matter particles due to the LMC, leads to an additional increase in $\Delta\eta$. When combined, these factors – the influx of high speed LMC particles and the acceleration of native Milky Way dark matter particles – contribute to a shift of more than 150 km/s in the high speed tail of the halo integrals, at the present day. This shift is a clear indicator of the dynamic interactions between the LMC and the Milky Way and their profound effects on the distribution and behavior of dark matter particles.

4. The influence of the LMC on the high speed tail of the halo integrals has profound implications for direct dark matter detection experiments. These experiments, which aim to identify the dark matter particles, rely heavily on accurate predictions of the local dark matter behavior, including speed and distribution. The presence of the LMC introduces significant modifications in these distributions, primarily manifested as

shifts in the expected exclusion limits for detecting dark matter. These shifts are oriented towards lower cross sections and smaller dark matter masses, broadening the scope of detection capabilities. Specifically, in the realm of future xenon-based experiments, the impact of the LMC is substantial. It lowers the exclusion limits for the dark matter-nucleon cross section by an order of magnitude for dark matter masses ~ 8 GeV, and even more dramatically for lower masses - more than three orders of magnitude for a dark matter mass of ~ 6 GeV, and over five orders for ~ 5 GeV. The germanium-based experiments are similarly affected, with the LMC's influence lowering the exclusion limits by an order of magnitude for dark matter masses ~ 0.5 GeV, and beyond three orders for ~ 0.4 GeV. In the case of silicon-based experiments, which focus on the dark matter-electron cross section, the impact is marked by a reduction in exclusion limits up to a factor of around 4 for dark matter masses ~ 1 MeV, and as much as 50 for 0.6 MeV. Additionally, there is a notable horizontal shift in these exclusion limits towards smaller dark matter masses, becoming more pronounced for lower masses. This shift extends across a range of materials used in experiments: a few GeV for xenon, several hundred MeV for germanium, and a fraction of an MeV for silicon. This horizontal shift is particularly critical as it signifies the LMC's role in extending the parameter space probed by these direct detection experiments towards lower dark matter masses. The ability to detect smaller dark matter masses enhances the potential for discovering new aspects of dark matter and its interactions, thus providing a broader understanding of this enigmatic component of the universe.

Our study unveils a novel finding: the LMC's significant influence on the local dark matter distribution is clearly evident even within a fully cosmological simulation that traces the evolution of Milky Way and LMC analogues. Despite the inherent halo-to-halo variations characteristic of cosmological simulations, a detailed examination of various snapshots of a specific Milky Way-LMC analogue yields several key insights. Paramount among these is the

observation that a massive satellite, that has just passed its pericentric approach, can significantly boost the high speed tail of the local dark matter velocity distribution.

Additionally, our research highlights the importance of our unique Sun-LMC geometry. This specific Sun-LMC geometry is found to maximize the impact on the dark matter velocity distribution.

Our results agree with those from ref. [12], which investigated the LMC's effect on direct detection signals in a suite of idealized simulations of the LMC's orbit around the Milky Way. In agreement with our conclusions, they observed that for smaller dark matter masses, the LMC causes a substantial vertical shift of more than an order of magnitude in the exclusion limits on the dark matter-nucleon cross section towards smaller cross sections.

The outcomes of our fully cosmological simulations contribute significantly to the current understanding of the LMC's role in influencing the local dark matter distribution. They underscore the importance of considering the LMC's impact in the analysis of future dark matter direct detection data, particularly for lower dark matter masses. The implications of our results extend well beyond the scope of direct detection. They provide valuable insights into the validity and potential of idealized simulations in predicting phenomena such as the dark matter wake induced by the LMC in the galactic halo.

Looking forward, the advancements in cosmological simulations, especially those achieving higher resolution, are poised to play a crucial role. These future simulations are expected to precisely quantify the variations in the high speed tail of the local dark matter velocity distribution attributable to the LMC. The enhanced resolution in these simulations will be key to deepening our understanding of the complex dynamics governing dark matter distributions and their interactions with celestial bodies like the LMC, thereby contributing to a more comprehensive understanding of the universe's dark component.

References

[1] J. Aalbers *et al.*, "First Dark Matter Search Results from the LUX-ZEPLIN (LZ) Experiment," *Phys. Rev. Lett.*, vol. 131, no. 4, p. 041 002, 2023. DOI: 10.1103/PhysRevLett.131.041002. arXiv: 2207.03764 [hep-ex].

[2] P. A. R. Ade *et al.*, "Planck 2015 results. XIII. Cosmological parameters," *Astron. Astrophys.*, vol. 594, A13, 2016. DOI: 10.1051/0004-6361/201525830. arXiv: 1502.01589 [astro-ph.CO].

[3] N. Aghanim *et al.*, "Planck 2018 results. VI. Cosmological parameters," *Astron. Astrophys.*, vol. 641, A6, 2020, [Erratum: Astron.Astrophys. 652, C4 (2021)]. DOI: 10.1051/0004-6361/201833910. arXiv: 1807.06209 [astro-ph.CO].

[4] R. Agnese *et al.*, "Projected Sensitivity of the SuperCDMS SNOLAB experiment," *Phys. Rev. D*, vol. 95, no. 8, p. 082 002, 2017. DOI: 10.1103/PhysRevD.95.082002. arXiv: 1610.00006 [physics.ins-det].

[5] D. S. Akerib *et al.*, "LUX-ZEPLIN (LZ) Conceptual Design Report," Sep. 2015. arXiv: 1509.02910 [physics.ins-det].

[6] G. Are the Magellanic Clouds on their First Passage about the Milky Way? N. Kallivayalil, L. Hernquist, *et al.*, "Are the Magellanic Clouds on their First Passage about the Milky Way?" *Astrophys. J.*, vol. 668, pp. 949–967, 2007. DOI: 10.1086/521385. arXiv: astro-ph/0703196.

[7] E. Armengaud *et al.*, "Development of ^{100}Mo-containing scintillating bolometers for a high-sensitivity neutrinoless double-beta decay search," *Eur. Phys. J. C*, vol. 77, no. 11, p. 785, 2017. DOI: 10.1140/epjc/s10052-017-5343-2. arXiv: 1704.01758 [physics.ins-det].

[8] I. Arnquist *et al.*, "First Constraints from DAMIC-M on Sub-GeV Dark-Matter Particles Interacting with Electrons," *Phys. Rev. Lett.*, vol. 130, no. 17, p. 171 003, 2023. DOI: 10.1103/PhysRevLett.130.171003. arXiv: 2302.02372 [hep-ex].

[9] M. Bartelmann, "Gravitational lensing," *Classical and Quantum Gravity*, vol. 27, no. 23, p. 233 001, Nov. 2010. DOI: 10.1088/0264-9381/27/23/233001.

[10] B. Batell, M. Pospelov, A. Ritz, and Y. Shang, "Solar Gamma Rays Powered by Secluded Dark Matter," *Phys. Rev. D*, vol. 81, p. 075 004, 2010. DOI: 10.1103/PhysRevD.81.075004. arXiv: 0910.1567 [hep-ph].

[11] G. Bertone, N. Bozorgnia, J. S. Kim, *et al.*, "Identifying WIMP dark matter from particle and astroparticle data," *JCAP*, vol. 03, p. 026, 2018. DOI: 10.1088/1475-7516/2018/03/026. arXiv: 1712.04793 [hep-ph].

[12] G. Besla, A. Peter, and N. Garavito-Camargo, "The highest-speed local dark matter particles come from the Large Magellanic Cloud," *JCAP*, vol. 11, p. 013, 2019. DOI: 10.1088/1475-7516/2019/11/013. arXiv: 1909.04140 [astro-ph.GA].

[13] J. Billard, M. Boulay, S. Cebriá n, *et al.*, "Direct detection of dark matter—APPEC committee report∗," *Reports on Progress in Physics*, vol. 85, no. 5, p. 056 201, Apr. 2022. DOI: 10.1088/1361-6633/ac5754.

[14] M. Boylan-Kolchin, V. Springel, S. D. M. White, A. Jenkins, and G. Lemson, "Resolving cosmic structure formation with the millennium-ii simulation," *Monthly Notices of the Royal Astronomical Society*, vol. 398, no. 3, pp. 1150–1164, Sep. 2009, ISSN: 1365-2966. DOI: 10.1111/j.1365-2966.2009.15191.x. [Online]. Available: http://dx.doi.org/10.1111/j.1365-2966.2009.15191.x.

[15] N. Bozorgnia, F. Calore, M. Schaller, *et al.*, "Simulated Milky Way analogues: implications for dark matter direct searches," *JCAP*, vol. 05, p. 024, 2016. DOI: 10.1088/1475-7516/2016/05/024. arXiv: 1601.04707 [astro-ph.CO].

[16] N. Bozorgnia, A. Fattahi, C. S. Frenk, *et al.*, "The dark matter component of the Gaia radially anisotropic substructure," *JCAP*, vol. 07, p. 036, 2020. DOI: 10.1088/1475-7516/2020/07/036. arXiv: 1910.07536 [astro-ph.GA].

[17] T. Bringmann *et al.*, "DarkBit: A GAMBIT module for computing dark matter observables and likelihoods," *Eur. Phys. J. C*, vol. 77, no. 12, p. 831, 2017. DOI: 10.1140/epjc/s10052-017-5155-4. arXiv: 1705.07920 [hep-ph].

[18] A. G. A. Brown *et al.*, "Gaia Data Release 2: Summary of the contents and survey properties," *Astron. Astrophys.*, vol. 616, A1, 2018. DOI: 10.1051/0004-6361/201833051. arXiv: 1804.09365 [astro-ph.GA].

[19] T. Callingham, M. Cautun, A. J. Deason, *et al.*, "The mass of the Milky Way from satellite dynamics," Aug. 2018. DOI: 10.1093/mnras/stz365. arXiv: 1808.10456 [astro-ph.GA].

[20] N. Castelló-Mor, "DAMIC-M Experiment: Thick, Silicon CCDs to search for Light Dark Matter," *Nucl. Instrum. Meth. A*, vol. 958, M. Krammer, T. Bergauer, M. Dragicevic, *et al.*, Eds., p. 162 933, 2020. DOI: 10.1016/j.nima.2019.162933. arXiv: 2001.01476 [physics.ins-det].

[21] D. G. Cerdeño, M. Fairbairn, T. Jubb, P. A. N. Machado, A. C. Vincent, and C. Bœhm, "Physics from solar neutrinos in dark matter direct detection experiments," *JHEP*, vol. 05, p. 118, 2016, [Erratum: JHEP 09, 048 (2016)]. DOI: 10.1007/JHEP09(2016)048. arXiv: 1604.01025 [hep-ph].

[22] K. Donaldson, M. S. Petersen, and J. Peñarrubia, "Effects on the local dark matter distribution due to the large magellanic cloud," *Mon. Not. Roy. Astron. Soc.*, vol. 513, no. 1, pp. 46–51, 2022. DOI: 10.1093/mnrasl/slac031. arXiv: 2111.15440 [astro-ph.GA].

[23] A. K. Drukier, K. Freese, and D. N. Spergel, "Detecting Cold Dark Matter Candidates," *Phys. Rev. D*, vol. 33, pp. 3495–3508, 1986. DOI: 10.1103/PhysRevD.33.3495.

[24] D. Erkal, V. Belokurov, C. F. P. Laporte, *et al.*, "The total mass of the large magellanic cloud from its perturbation on the orphan stream," *Monthly Notices of the Royal Astronomical Society*, vol. 487, no. 2, pp. 2685–2700, May 2019. DOI: 10.1093/mnras/stz1371. [Online]. Available: https://doi.org/10.1093%2Fmnras%2Fstz1371.

[25] R. Essig, J. Mardon, and T. Volansky, "Direct Detection of Sub-GeV Dark Matter," *Phys. Rev. D*, vol. 85, p. 076 007, 2012. DOI: 10.1103/PhysRevD.85.076007. arXiv: 1108.5383 [hep-ph].

[26] N. W. Evans, C. A. J. O'Hare, and C. McCabe, "Refinement of the standard halo model for dark matter searches in light of the Gaia Sausage," *Phys. Rev. D*, vol. 99, no. 2, p. 023 012, 2019. DOI: 10.1103/PhysRevD.99.023012. arXiv: 1810.11468 [astro-ph.GA].

[27] B. Famaey and S. S. McGaugh, "Modified newtonian dynamics (MOND): Observational phenomenology and relativistic extensions," *Living Reviews in Relativity*, vol. 15, no. 1, Sep. 2012. DOI: 10.12942/lrr-2012-10.

[28] N. Garavito-Camargo, G. T. highest-speed local dark matter particles come from the Large Magellanic Cloud, C. F. P. Laporte, *et al.*, "Quantifying the impact of the large magellanic cloud on the structure of the milky way's dark matter halo using basis function expansions," *The Astrophysical Journal*, vol. 919, no. 2, p. 109, Sep. 2021. DOI: 10.3847/1538-4357/ac0b44.

[29] G. Gelmini and P. Gondolo, "WIMP annual modulation with opposite phase in Late-Infall halo models," *Phys. Rev. D*, vol. 64, p. 023 504, 2001. DOI: 10.1103/PhysRevD.64.023504. arXiv: hep-ph/0012315.

[30] G. Gelmini and P. Gondolo, *Dm production mechanisms*, 2010. arXiv: 1009.3690 [astro-ph.CO].

[31] P. Giannozzi, S. Baroni, N. Bonini, *et al.*, "Quantum espresso: A modular and open-source software project for quantum simulations of materials," *Journal of Physics: Condensed Matter*, vol. 21, no. 39, p. 395 502, Sep. 2009, ISSN: 1361-648X. DOI: 10.1088/0953-8984/21/39/395502. [Online]. Available: http://dx.doi.org/10.1088/0953-8984/21/39/395502.

[32] F. A. Gómez, G. Besla, D. D. Carpintero, Á. Villalobos, B. W. O'Shea, and E. F. Bell, "And yet it moves: The dangers of artificially fixing the Milky Way center of mass in the presence of a massive Large Magellanic Cloud," *Astrophys. J.*, vol. 802, no. 2, p. 128, 2015. DOI: 10.1088/0004-637X/802/2/128. arXiv: 1408.4128 [astro-ph.GA].

[33] F. A. Gómez, R. J. J. Grand, A. Monachesi, *et al.*, "Lessons from the Auriga discs: The hunt for the Milky Way's ex-situ disc is not yet over," *Mon. Not. Roy. Astron. Soc.*, vol. 472, no. 3, pp. 3722–3733, 2017. DOI: 10.1093/mnras/stx2149. arXiv: 1704.08261 [astro-ph.GA].

[34] F. A. Gómez, S. D. M. White, F. Marinacci, *et al.*, "A fully cosmological model of a monoceros-like ring," *Monthly Notices of the Royal Astronomical Society*, vol. 456, no. 3, pp. 2779–2793, Dec. 2015, ISSN: 1365-2966. DOI: 10.1093/mnras/stv2786. [Online]. Available: http://dx.doi.org/10.1093/mnras/stv2786.

[35] R. J. J. Grand, F. A. Gómez, F. Marinacci, *et al.*, "The Auriga Project: the properties and formation mechanisms of disc galaxies across cosmic time," *Mon. Not. Roy. Astron. Soc.*, vol. 467, no. 1, pp. 179–207, 2017. DOI: 10.1093/mnras/stx071. arXiv: 1610.01159 [astro-ph.GA].

[36] P. D. Group, P. A. Zyla, R. M. Barnett, *et al.*, "Review of Particle Physics," *Progress of Theoretical and Experimental Physics*, vol. 2020, no. 8, p. 083C01, Aug. 2020, ISSN: 2050-3911. DOI: 10.1093/ptep/ptaa104. eprint: https://academic.oup.com/ptep/article-pdf/2020/8/083C01/34673722/ptaa104.pdf. [Online]. Available: https://doi.org/10.1093/ptep/ptaa104.

[37] R. H. Helm, "Inelastic and Elastic Scattering of 187-Mev Electrons from Selected Even-Even Nuclei," *Phys. Rev.*, vol. 104, pp. 1466–1475, 1956. DOI: 10.1103/PhysRev.104.1466.

[38] P. F. Hopkins, D. Kereš, J. Oñorbe, *et al.*, "Galaxies on FIRE (Feedback In Realistic Environments): stellar feedback explains cosmologically inefficient star formation," *Monthly Notices of the Royal Astronomical Society*, vol. 445, no. 1, pp. 581–603, Sep. 2014, ISSN: 0035-8711. DOI: 10.1093/mnras/stu1738. eprint: https://academic.oup.com/mnras/article-pdf/445/1/581/18473138/stu1738.pdf. [Online]. Available: https://doi.org/10.1093/mnras/stu1738.

[39] A. Jenkins, "A new way of setting the phases for cosmological multiscale gaussian initial conditions," *Monthly Notices of the Royal Astronomical Society*, vol. 434, no. 3, pp. 2094–2120, Jul. 2013. DOI: 10.1093/mnras/stt1154. [Online]. Available: https://doi.org/10.1093%2Fmnras%2Fstt1154.

[40] G. Jungman, M. Kamionkowski, and K. Griest, "Supersymmetric dark matter," *Physics Reports*, vol. 267, no. 5-6, pp. 195–373, Mar. 1996. DOI: 10.1016/0370-1573(95)00058-5.

[41] F. Kahlhoefer, S. Kulkarni, and S. Wild, "Exploring light mediators with low-threshold direct detection experiments," *JCAP*, vol. 11, p. 016, 2017. DOI: 10.1088/1475-7516/2017/11/016. arXiv: 1707.08571 [hep-ph].

[42] N. Kallivayalil, R. P. van der Marel, G. Besla, J. Anderson, and C. Alcock, "Third-Epoch Magellanic Cloud Proper Motions I: HST/WFC3 data and Orbit Implications," *Astrophys. J.*, vol. 764, p. 161, 2013. DOI: 10.1088/0004-637X/764/2/161. arXiv: 1301.0832 [astro-ph.CO].

[43] S. J. Lee, B. Kilminster, and A. Macchiolo, "Dark Matter in CCDs at Modane (DAMIC-M) : A silicon detector apparatus searching for low-energy physics processes," *JINST*, vol. 15, no. 02, M. Nessi, Ed., p. C02050, 2020. DOI: 10.1088/1748-0221/15/02/C02050. arXiv: 2001.01209 [physics.ins-det].

[44] R. P. van der Marel, D. R. Alves, E. Hardy, and N. B. Suntzeff, "New understanding of large magellanic cloud structure, dynamics and orbit from carbon star kinematics," *Astron. J.*, vol. 124, pp. 2639–2663, 2002. DOI: 10.1086/343775. arXiv: astro-ph/0205161.

[45] F. Marinacci, R. Pakmor, and V. Springel, "The formation of disc galaxies in high resolution moving-mesh cosmological simulations," *Mon. Not. Roy. Astron. Soc.*, vol. 437, no. 2, pp. 1750–1775, 2014. DOI: 10.1093/mnras/stt2003. arXiv: 1305.5360 [astro-ph.CO].

[46] J. F. Navarro, A. Ludlow, V. Springel, *et al.*, "The Diversity and Similarity of Cold Dark Matter Halos," *Mon. Not. Roy. Astron. Soc.*, vol. 402, p. 21, 2010. DOI: 10.1111/j.1365-2966.2009.15878.x. arXiv: 0810.1522 [astro-ph].

[47] L. Necib, M. Lisanti, and V. Belokurov, "Inferred Evidence For Dark Matter Kinematic Substructure with SDSS-Gaia," Jul. 2018. DOI: 10.3847/1538-4357/ab095b. arXiv: 1807.02519 [astro-ph.GA].

[48] K. C. Y. Ng, J. F. Beacom, A. H. G. Peter, and C. Rott, "Solar Atmospheric Neutrinos: A New Neutrino Floor for Dark Matter Searches," *Phys. Rev. D*, vol. 96, no. 10, p. 103 006, 2017. DOI: 10.1103/PhysRevD.96.103006. arXiv: 1703.10280 [astro-ph.HE].

[49] C. A. J. O'Hare, N. W. Evans, C. McCabe, G. Myeong, and V. Belokurov, "Velocity substructure from Gaia and direct searches for dark matter," *Phys. Rev. D*, vol. 101, no. 2, p. 023 006, 2020. DOI: 10.1103/PhysRevD.101.023006. arXiv: 1909.04684 [astro-ph.GA].

[50] *Particle Dark Matter: Observations, Models and Searches*. Cambridge University Press, 2010. DOI: 10.1017/CBO9780511770739.

[51] M. Pato, F. Iocco, and G. Bertone, "Dynamical constraints on the dark matter distribution in the milky way," *Journal of Cosmology and Astroparticle Physics*, vol. 2015, no. 12, pp. 001–001, Dec. 2015. DOI: 10.1088/1475-7516/2015/12/001. [Online]. Available: https://doi.org/10.1088%2F1475-7516%2F2015%2F12%2F001.

[52] C. Power, J. F. Navarro, A. Jenkins, *et al.*, "The inner structure of CDM haloes – i. a numerical convergence study," *Monthly Notices of the Royal Astronomical Society*, vol. 338, no. 1, pp. 14–34, Jan. 2003. DOI: 10.1046/j.1365-8711.2003.05925.x.

[53] A. Robertson, R. Massey, and V. Eke, "What does the Bullet Cluster tell us about self-interacting dark matter?" *Mon. Not. Roy. Astron. Soc.*, vol. 465, no. 1, pp. 569–587, 2017. DOI: 10.1093/mnras/stw2670. arXiv: 1605.04307 [astro-ph.CO].

[54] P. Salati, F. Donato, and N. Fornengo, "Indirect Dark Matter Detection with Cosmic Antimatter," pp. 521–546, Mar. 2010. arXiv: 1003.4124 [astro-ph.HE].

[55] M. Salem, G. Besla, G. Bryan, M. Putman, R. P. van der Marel, and S. Tonnesen, "RAM PRESSURE STRIPPING OF THE LARGE MAGELLANIC CLOUD's DISK AS a PROBE OF THE MILKY WAY's CIRCUMGALACTIC MEDIUM," *The Astrophysical Journal*, vol. 815, no. 1, p. 77, Dec. 2015. DOI: 10.1088/0004-637x/815/1/77.

[56] I. M. E. Santos-Santos, A. Fattahi, L. V. Sales, and J. F. Navarro, "Magellanic satellites in ΛCDM cosmological hydrodynamical simulations of the Local Group," *Mon. Not. Roy. Astron. Soc.*, vol. 504, no. 3, pp. 4551–4567, 2021. DOI: 10.1093/mnras/stab1020. arXiv: 2011.13500.

[57] D. Sarkar, J. Flitter, and E. D. Kovetz, "Exploring delaying and heating effects on the 21-cm signature of fuzzy dark matter," *Phys. Rev. D*, vol. 105, no. 10, p. 103 529, 2022. DOI: 10.1103/PhysRevD.105.103529. arXiv: 2201.03355 [astro-ph.CO].

[58] M. Schaller, C. S. Frenk, A. Fattahi, J. F. Navarro, K. A. Oman, and T. Sawala, "The low abundance and insignificance of dark discs in simulated Milky Way galaxies," *Mon. Not. Roy. Astron. Soc.*, vol. 461, no. 1, pp. L56–L61, 2016. DOI: 10.1093/mnrasl/slw101. arXiv: 1605.02770 [astro-ph.GA].

[59] J. Schaye, R. A. Crain, R. G. Bower, *et al.*, "The EAGLE project: simulating the evolution and assembly of galaxies and their environments,", vol. 446, no. 1, pp. 521–554, Jan. 2015. DOI: 10.1093/mnras/stu2058. arXiv: 1407.7040 [astro-ph.GA].

[60] A. Smith-Orlik *et al.*, "The impact of the Large Magellanic Cloud on dark matter direct detection signals," Feb. 2023. arXiv: 2302.04281 [astro-ph.GA].

[61] Y. Sofue, M. Honma, and T. Omodaka, "Unified rotation curve of the galaxy — decomposition into de vaucouleurs bulge, disk, dark halo, and the 9-kpc rotation dip —," *Publications of the Astronomical Society of Japan*, vol. 61, no. 2, pp. 227–236, Apr. 2009. DOI: 10.1093/pasj/61.2.227.

[62] V. Springel, "E pur si muove: Galiliean-invariant cosmological hydrodynamical simulations on a moving mesh," *Mon. Not. Roy. Astron. Soc.*, vol. 401, p. 791, 2010. DOI: 10.1111/j.1365-2966.2009.15715.x. arXiv: 0901.4107 [astro-ph.CO].

[63] V. Springel, S. D. M. White, G. Tormen, and G. Kauffmann, "Populating a cluster of galaxies. 1. Results at z = 0," *Mon. Not. Roy. Astron. Soc.*, vol. 328, p. 726, 2001. DOI: 10.1046/j.1365-8711.2001.04912.x. arXiv: astro-ph/0012055.

[64] H. J. de Vega and N. G. Sanchez, "Warm Dark Matter Galaxies with Central Supermassive Black Holes," *Universe*, vol. 8, no. 3, p. 154, 2022. DOI: 10.3390/universe8030154. arXiv: 1705.05418 [astro-ph.GA].

[65] M. Vogelsberger, S. Genel, V. Springel, *et al.*, "Properties of galaxies reproduced by a hydrodynamic simulation,", vol. 509, no. 7499, pp. 177–182, May 2014. DOI: 10.1038/nature13316. arXiv: 1405.1418 [astro-ph.CO].

[66] D. G. York, J. Adelman, J. John E. Anderson, *et al.*, "The sloan digital sky survey: Technical summary," *The Astronomical Journal*, vol. 120, no. 3, pp. 1579–1587, Sep. 2000. DOI: 10.1086/301513.